ABSTRACT

Title of Thesis:	NUMERICAL/EXPERIMENTAL HYBRID APPROACH TO PREDICT SUBSTRATE WARPAGE
	Byung Yub Kim Master of Science 2018
Thesis Directed By:	Professor Bongtae Han Department of Mechanical Engineering

A hybrid approach is proposed to enhance warpage predictability of thin advanced substrates. Experimental warpage data of thin advanced substrates is first obtained under various conditions. High sensitivity measurements (a contour interval of 6.25 microns/fringe or equivalent to shadow moiré with a grating of 160 lines/mm) without painting the surface becomes possible through the advanced shadow moiré method called Shadow Moiré with Non-zero Talbot distance (SM-NT) in conjunction with the optical/digital fringe multiplication (O/DFM) method. The measured warpage is combined with an FEA approach called trace mapping to incorporate the effect of the copper trace layouts into the analysis. A hybrid model is created through calibration of the properties most critical to warpage, and the warpage values of the substrates at reflow temperatures are predicted.

NUMERICAL/EXPERIMENTAL HYBRID APPROACH TO PREDICT SUBSTRATE WARPAGE

by

Byung Yub Kim

Thesis submitted to the Faculty of the Graduate School of the
University of Maryland, College Park, in partial fulfillment
of the requirements for the degree of
Master of Science
2018

Advisory Committee:
Professor Bongtae Han, Chair
Professor Abhijit Dasgupta
Professor Patrick McCluskey

© Copyright by
Byung Yub Kim
2018

Acknowledgements

First, I would like to give my immense appreciation to my advisor, Professor Bongtae Han. His mentorship and teachings were invaluable throughout my research, and will continue to guide me throughout my career. I will forever be grateful for the care and patience that he showed me and I could not have asked for a better mentor; he knew how to challenge my limits and broaden my way of thinking. Thank you again for the past few years.

In addition, I would like to thank Dr. Abhijit Dasgupta and Dr. Patrick McCluskey for serving on my thesis committee and for their helpful comments regarding my research.

I also want to thank all of the lab group members I interacted with at LOMSS: Michelle Kim, Dr. Dae-Suk Kim, Dr. Kenny Mahan, Dr. Yong Sun, Sean Wei, Bulong Wu, Hyun-Seop Lee, Jack Yang, Ryan Kim, and Artur Roman. We had countless memorable times together inside and outside of the lab and I will not forget the experiences that we shared.

Finally, I want to thank all of my friends and family members who offered me support throughout the last couple of years, especially my Mom, Dad, and sister.

Table of Contents

List of Figures

Chapter 1: Introduction

1.1. Background

The evolution of mobile devices as integral societal items accelerated the pace of the semiconductor industry. Technological advancements no longer set the pace of new devices; instead, innovation is driven by consumer wants and needs [1-5]. There is a constant demand for smaller and more efficient items, making form factor, time, and cost more critical than ever. This drive has accelerated the pace for substrate manufacturers; they are forced to constantly update their designs for thinner and more advanced substrates.

According to Khandpur [6], printed circuit boards have been the traditional choice for electronic packaging substrates since the 1970s. They are made from a copper clad laminate core with additional layers of copper and prepreg, or partially cured epoxy resin, stacked together. The laminate is comprised of glass fiberglass cloths embedded in an epoxy resin and is flanked by two layers of copper. Traces are drawn into the copper layers for signal routing, which are held together with prepreg [6]. After lamination at high pressure and temperatures, the board functions as the package base. A schematic of a printed circuit board is shown in Figure 1.

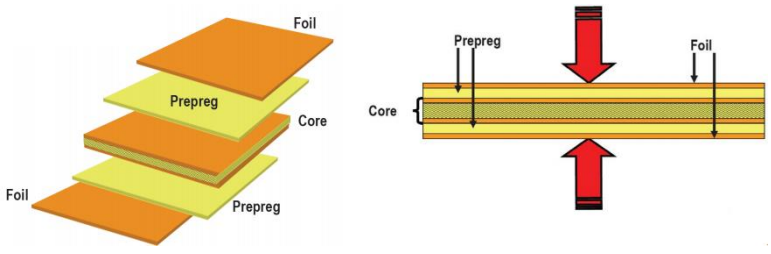

Figure 1. Printed circuit board schematic [7]

However, as flip chip technology matured, printed circuit boards had to adapt to match the increase in signal density and decrease in pitch. Underfill could be used to alleviate the issues with coefficient of thermal expansion (CTE) mismatches between the solder and organic material but the high density terminals of the flip chip necessitated substrate changes [8]. This was achieved through the surface laminar circuit layer (also called the build-up layer), which was first introduced by IBM in the 1990s [9]. The premise was to minimize the thickness of the additional dielectric and copper layers by etching and plating them directly on top of a core. The general procedure is shown in Figure 2. Dielectric layers are coated on top of a copper clad laminate, and additional interconnections are added in through lithography and copper plating. The resulting layers are thin and are capable of providing high density pathways for flip chips as illustrated in Figure 3.

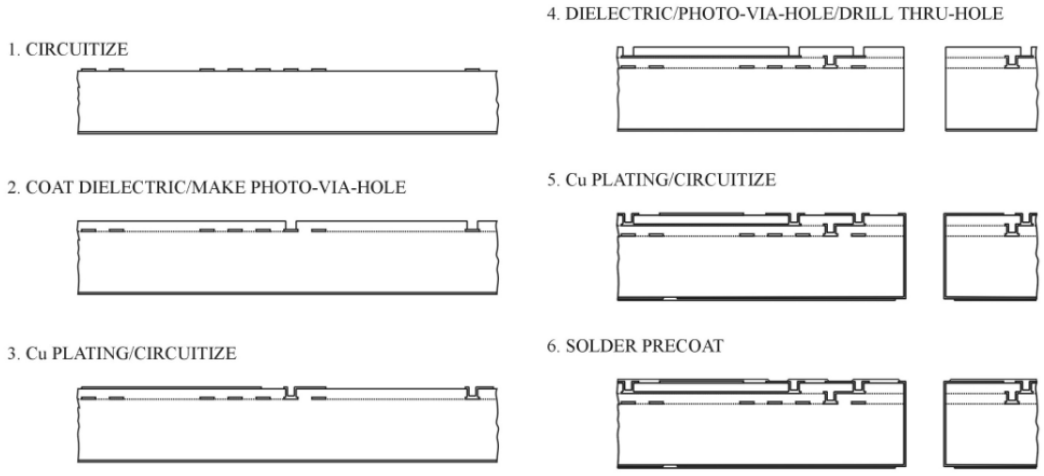

Figure 2. Surface laminar circuit procedure [9]

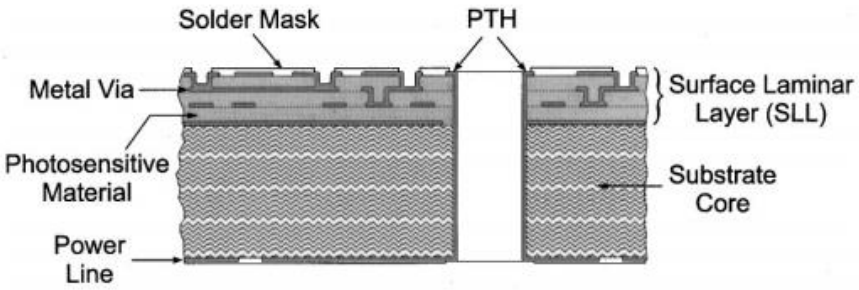

Figure 3. PCB schematic with surface laminar circuit layer [10]

However, with the rising demand for miniaturized products, substrate technology had to continually evolve for increased space efficiency. Embedded and coreless substrates are two approaches to decrease the thickness of the substrate, where components are incorporated into the layers or the core is removed entirely and the substrate consists solely of the surface laminar circuit layers, respectively. Example of a coreless embedded trace substrate (ETS) is displayed in Figure 4.

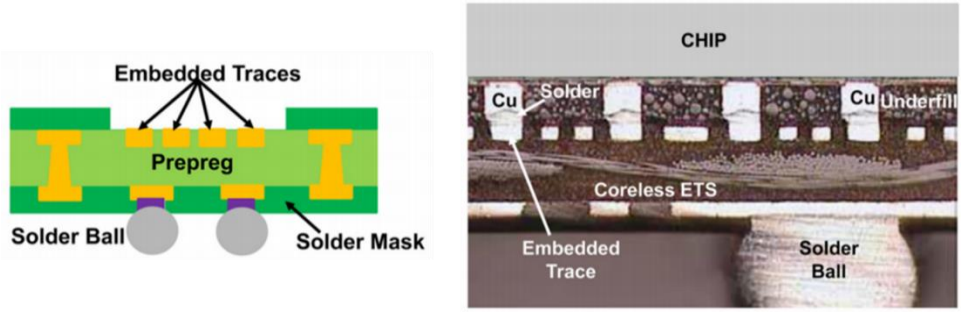

(a) (b)

Figure 4. Schematics of a coreless ETS (a) schematic (b) cross section [11]

These designs enable substrate thicknesses as thin as 100 μm, with additional benefits such as superior electrical performance, signal integrity, and design flexibility when compared to conventional substrates [12-15]. Continued improvements are necessary to match consumer expectations of new electronic packages and devices.

1.2. Motivation

Warpage of electronic packaging substrates has always been critical due to possible reliability and yield concerns during package assembly. Previously, substrates only had minor issues with warpage due to their thickness and rigidity, as their high bending stiffness minimized potential errors. Thinner substrates pose a new set of challenges as the decreases in rigidity have exacerbated substrate warpage [2-5, 12-17]. As a result, the thermal warpage of new thin and advanced substrates must be carefully examined.

Modeling is a common technique for studying and improving the warpage of thin and advanced substrates. It can massively reduce the time to analyze and solve warpage issues without the need for continuous design of experiments (DOE). Given the multitude of parameters that affect warpage (e.g. the copper trace layout, material properties, thicknesses), DOE is unable to consider all of these in a timely manner [2, 3, 5, 18-21]. Predictive modeling is necessary to efficiently accommodate all of the substrate properties and their inherent deviations.

With thicker substrates, simulations could be simplified by treating layers as homogeneous or transversely isotropic layers [2, 5, 22, 23]. These approximations were valid because the traces were an insignificant portion of the total board. The reduced bending stiffness for new substrates, combined with the naturally high CTE and modulus of Cu, make the previous simplifications produce more uncertainties in warpage predictions [2, 5]. Therefore, an improved modeling methodology is required to consider the impact of the microstructure layouts in these substrates.

However, simulations have their own limitations. Although the details of Cu traces can be included in the model, accurate prediction of the warpage through simulations alone is still extremely challenging. In addition to the temperature and time-dependent material properties of polymeric materials used in substrates, direct modeling of the traces requires extreme computational resources. Very often, the number of elements is limited in the modeling when the thinnest trace (~ 15 μm) is incorporated, leading to computational issues related to material discontinuities. More critically, the stress-free temperature of substrates is not readily definable, which is critical for determining absolute topography. As a result, modeling is insufficient by itself to accurately predict warpage; experimental results are necessary to improve its capabilities.

A hybrid approach is proposed to cope with the above challenges. Experimental warpage data of substrates are first obtained under various conditions without coating surfaces with a matte white paint. High sensitivity measurements (a contour interval of 6.25 μm/fringe or equivalent to shadow moiré with a grating of 160 lines/mm) without painting becomes possible through the advanced shadow moiré method called Shadow Moiré with Non-zero Talbot distance (SM-NT) in conjunction with the optical/digital fringe multiplication (O/DFM) method. The measured warpage are combined with an FEA approach called trace mapping to incorporate the effect of the copper trace layouts into the analysis. A hybrid model is created through calibration of the properties most critical to warpage, and the warpage values of the substrates at reflow temperature are predicted.

Chapter 2: Warpage Measurement by Shadow Moiré with Non-Zero Talbot Distance

2.1. Shadow Moiré with Non-Zero Talbot Distance (SM-NT) Theory

Shadow moiré is an optical technique for measuring out-of-plane displacements. Fringes representing surface topography are produced by geometric interference between a reference grating and its shadow on the specimen. This method requires a reference grating, a light source, and a camera; these items and their setup with respect to the specimen governs the sensitivity of the measurement. It was first introduced by Meadows et al. and Takasaki in 1970 and is commonly employed for topographical measurements within the semiconductor industry [24, 25]. It is the chosen experimental method to measure warpage for this study.

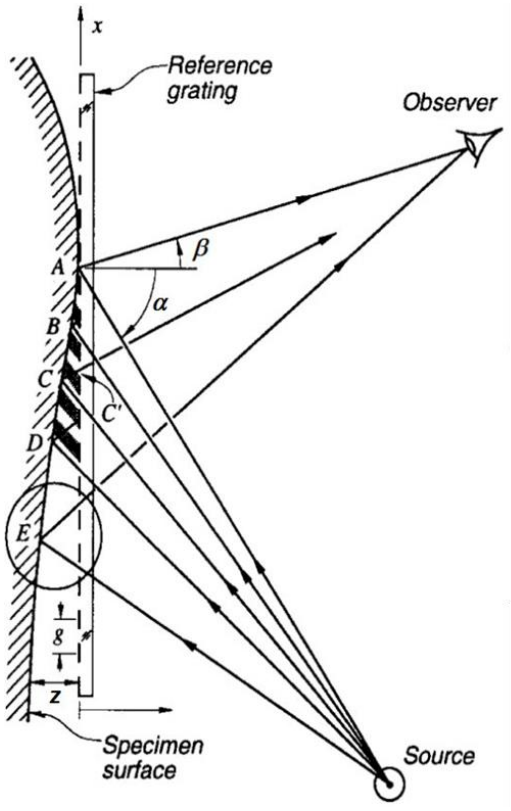

Figure 5. Shadow moiré configuration [26]

An example of a generic shadow moiré configuration can be seen in

Figure 5 where z is the gap between the reference grating and the specimen; g is the pitch of the reference grating; and α and β are the angles of the light source and camera relative to the grating normal, respectively. The four ingredients are the reference grating, source, observer, and specimen. The reference gratings are typically Ronchi gratings, which are comprised of alternating bands of transparent and opaque bars of equal width. These gratings are generally produced by depositing metal layers (e.g. chrome) on one side of a transparent layer, such as fused silica. The source refers to a light source, and is not limited to a specific type or model [27-30]. Typically, point or line light sources are used to concentrate the light and avoid loss through diffraction. The observer is a camera to capture fringes and should be selected based on the field of view and resolution required.

The warpage of the specimen is evaluated at locations with respect to a reference point. In Figure 5, the specimen and reference grating have contact at point A. This will be chosen as the reference point. With $z = 0$, point A is given the fringe order $N = 0$. There would be a bright fringe at this location because light passes through the transparent bars of the grating and reflects directly into the camera. Points C and E would also have bright fringes. On the other hand, point B and F would appear as black fringes because light reaches the specimen and reflects from those points but is blocked by the opaque regions of the grating. The fringe order is calculated by where the light hits and exits the region. For example, light reaches point C four fringes from point A, but it exits towards the camera three fringes from point A. Point C is given the fringe order 1 based on the difference between the number of fringes between point A and C,

and point A and C'. This relationship is geometrically evaluated with g, α, and β to form the relationship between warpage and fringe order:

$$z(x, y) = \frac{g}{\tan\alpha + \tan\beta} N(x, y). \quad (1)$$

The sensitivity of shadow moiré, which is also called the contour interval, is defined from the relationship above as

$$\Gamma = \frac{g}{\tan\alpha + \tan\beta}. \quad (2)$$

The contour interval is a function of the grating pitch and the light source and observer angles. It must be noted that in Figure 5, depending on the x-position of the specimen, both α and β will change through the width of the specimen, which would result in inconsistent sensitivities. There are two types of arrangements that resolve this issue. The first one keeps tan(α) + tan(β) constant by requiring the light source and observer to be the same distance away from the specimen, as shown in Figure 6, resulting in the geometric configuration below:

$$\tan\alpha + \tan\beta = \frac{D}{L + z} \approx \frac{D}{L}. \quad (3)$$

D is the distance between the light source and observer, and L is the distance between either of them to the specimen. This constraint assumes that z is negligible, which is reasonable given that z is generally orders of magnitude smaller than L. With this, the contour interval will be constant:

$$\Gamma = \frac{g}{\tan\alpha + \tan\beta} = \frac{gL}{D}. \quad (4)$$

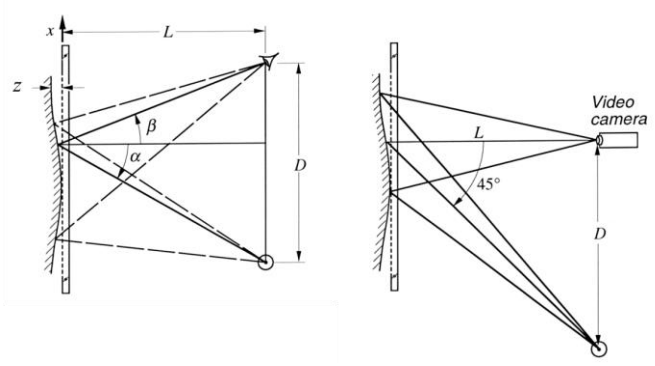

(a) (b)

Figure 6. Shadow moiré configuration with constant sensitivity: tan α + tan β = constant, (a) oblique viewing, (b) normal viewing [26]

The second arrangement aims at keeping the angles constant through the use of collimated beams. Figure 7 shows two setups using plano-convex lenses for collimated light. Light is collimated before it can reach the specimen and diffuse light from the specimen is collimated before being captured by the observer. Although this setup can be advantageous because the source and observer positions are not limited and enables compact systems, it is restricted by the size of the collimating lenses.

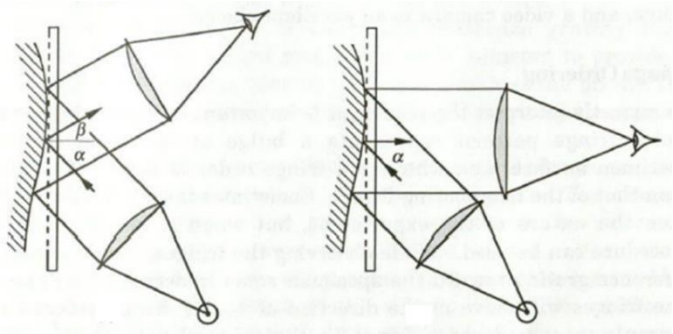

(a) (b)

Figure 7. Shadow moiré configuration with constant sensitivity: α and β are constant, (a) oblique viewing, (b) normal viewing [26]

2.1.1. Talbot Distance

Equation 1 is slightly misleading because it implies that fringes will be produced for all values of *z*. In reality, the visibility of fringe patterns changes cyclically as *z* changes, which is a result of the Talbot effect or the grating self-imaging effect. When a monochromatic collimated light shines on an amplitude grating, the rays are divided and diffracted into multiple beams. At certain distances from the grating, the diffracted beams will interfere with each other to create exact replicas of the same grating, as depicted in Figure 8. The frequency will remain the same. As Talbot was the first person to observe this, this optical phenomenon was named after him and virtual gratings are referred to as "Talbot images" [31]. The distance between these virtual gratings is referred to as the Talbot distance and can be expressed as

$$D_T^{\alpha} = \frac{g^2}{\lambda}. \tag{5}$$

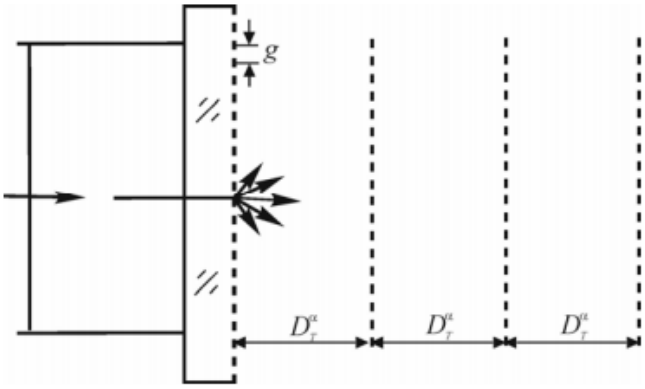

Figure 8. Schematic of virtual gratings being formed at Talbot distances

Patterns are still produced between the Talbot distances but are not replicas of the initial reference grating. A complementary image of the grating (or 180° phase shifted image) forms at ½ of the Talbot distance and the images disappear entirely at

¼ and ¾ of the Talbot distance due to destructive interference [26]. Given that shadow moiré typically uses oblique illumination, the Talbot distance equation determined by Testorf is conventionally used [32]

$$D_T^{\alpha} = \frac{2g^2}{\lambda}\cos^3\alpha. \tag{6}$$

The virtual images from oblique illumination are shown in Figure 9. It should be noted that because of the light source angle α, the virtual grating translates in the x direction by $z\tan(\alpha)$.

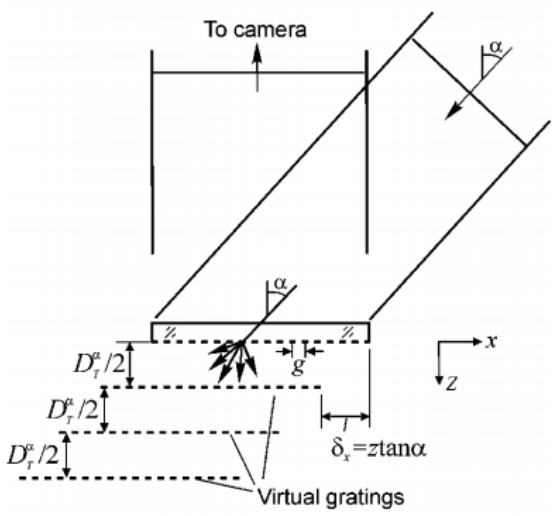

Figure 9. Virtual gratings formed from oblique illumination [33]

Shadow moiré relies on the fundamental assumption of rectilinear propagation of light for the geometric analysis above. However, if the gap z is small in comparison to the Talbot distance, this assumption can be considered valid and crisp shadows will be formed on the specimen surface from the reference grating [26]. Generally, the grating self-imaging distance will be several orders of magnitude larger than the gap. For example, if a 10 lines/mm grating is used (g = 100 μm) with a white light source (λ ~

550 nm) and α = 45°, β = 0°, the self-imaging distance would be roughly 18 mm while each fringe order would indicate 100 μm of warpage. Even if there were 10 fringes, *z* would be at max ~5% of the self-imaging distance, which is sufficiently small to assume rectilinear propagation.

2.1.2. Contrast

Fringe contrast is defined by how well one can distinguish the dark and bright fringes from each other. Mathematically, it can be expressed as

$$C = \frac{I^{\max} - I^{\min}}{I^{\max} + I^{\min}}. \tag{7}$$

For shadow moiré, it is a function of the contrasts from the Talbot effect (C_T) and from the aperture effect (C_A). As discussed above, the virtual grating will appear and disappear cyclically because of the Talbot effect. This effect from diffraction will cause contrast to vary with respect to *z*. Han numerically calculated the expected contrast as a function of *z* as

$$C_T(z) = \frac{I_s^{\max}(z) - I_s^{\min}(z)}{I_s^{\max}(z) + I_s^{\min}(z)} = 1 - 2\frac{\int_{\delta_x + g/2}^{\delta_x + g} I(x,z)dx}{\int_{\delta_x}^{\delta_x + g} I(x,z)dx} \tag{8}$$

which was confirmed experimentally [34]. This equation assumes that a pinhole aperture is used in order to define the intensity at various distances.

The fringe contrast will also be affected by the aperture of the imaging system. When the reflected light is blocked by the opaque bar from the reference grating, this location should produce a dark fringe. However, if the aperture is large enough, scattered light can bypass the opaque bar and enter the camera. As *z* increases, more

light will be able to enter the camera. These cases are shown in Figure 10. Part (b) depicts how a larger aperture will enable light from opaque regions of the reference grating to reach the camera. This dilutes the difference in intensities between the light and dark regions, resulting in lower contrast.

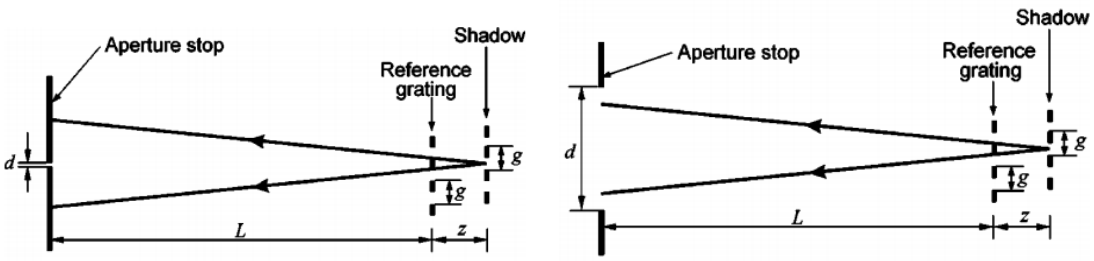

(a) (b)

Figure 10. Aperture effect schematic with (a) small aperture (b) large aperture [33]

The aperture effect on the contrast was determined through the contrast equation. The maximum and minimum intensities were calculated geometrically assuming a circular aperture and rectilinear propagation of light as

$$I_A^{\max}(z) = I_0\left(\frac{1}{2} - \frac{2d_e z}{3\pi g}\right),\ I_A^{\min}(z) = I_0\left(\frac{2d_e z}{3\pi g}\right)$$
$$C_A(z) = \frac{I_A^{\max}(z) - I_A^{\min}(z)}{I_A^{\max}(z) + I_A^{\min}(z)} = 1 - \frac{8d_e z}{3\pi g},\ 0 \le z \le \frac{3\pi g}{8d_e} \tag{9}$$

with d_e as the effective aperture, or the aperture diameter divided by the distance between the specimen and aperture. Combining the Talbot and aperture effects describes the final contrast of shadow moiré fringes as

$$C(z) = C_T(z) * C_A(z) = \left[1 - 2\frac{\int_{\delta_x+g/2}^{\delta_x+g} I(x,z)dx}{\int_{\delta_x}^{\delta_x+g} I(x,z)dx}\right]\left[1 - \frac{8d_e z}{3\pi g}\right],\ 0 \le z \le \frac{3\pi g}{8d_e} \tag{10}$$

Figure 11 shows the relationship between the fringe contrast and the normalized distance from the reference grating with both Talbot and aperture effects taken into consideration for g = 100 μm, α = 63.4°, β = 0°, d_e = 1/300, and a white light source. It should be noted that the dynamic range, or region with good contrast, is actually higher at ½ Talbot distance because it can use the areas on both sides of the peak. This region is nearly halved at the 0 Talbot distance.

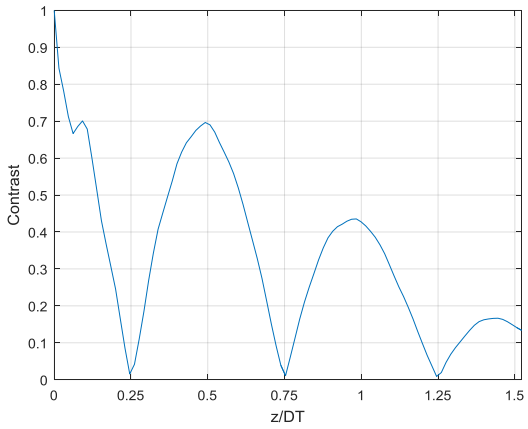

Figure 11. Fringe contrast vs normalized distance from the reference grating

Although fringe contrast is highest at the 0 Talbot distance, there are practical issues when fringes are measured for specimens with large warpages. There should be a sufficient gap between the grating and the specimen; otherwise, the specimen can touch the grating during measurements, which can alter the warpage values. Imaging at non-zero Talbot distances has the additional benefit of increasing the dynamic range. As noted above, because the area on both sides of the contrast peak can be used at non-zero Talbot distances, the dynamic range is near double the value at 0 Talbot. This is exemplified in Figure 12 where the fringe contrast along a tilted painted glass decreases after the 0 Talbot distance, and increases again at the ½ Talbot distance. It is evident

that the ½ Talbot distance has a larger region with good contrast than the 0 Talbot distance.

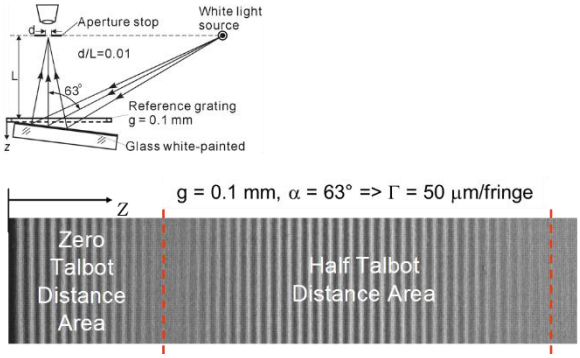

Figure 12. Illustration of the dynamic range at ½ Talbot distance with the setup [34]

2.2. Experimental Setup for Reflow Profile

An experimental shadow moiré with non-zero Talbot distance (SM-NT) setup was created to measure the warpage of the units during the reflow profile.

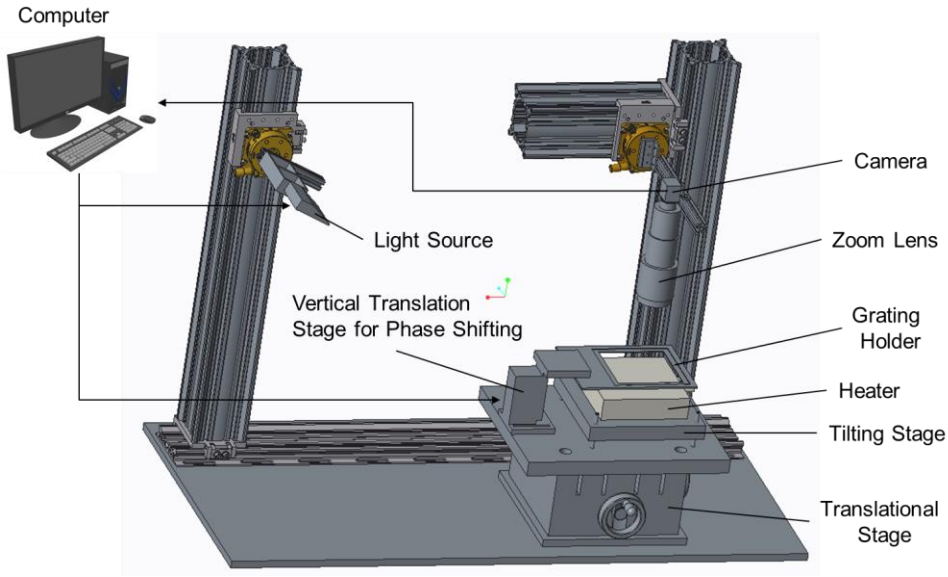

Figure 13. SM-NT Setup Schematic

2.2.1. Equipment

The schematic of the experimental setup is shown in Figure 13. Images of the actual setup are shown in Figure 14.

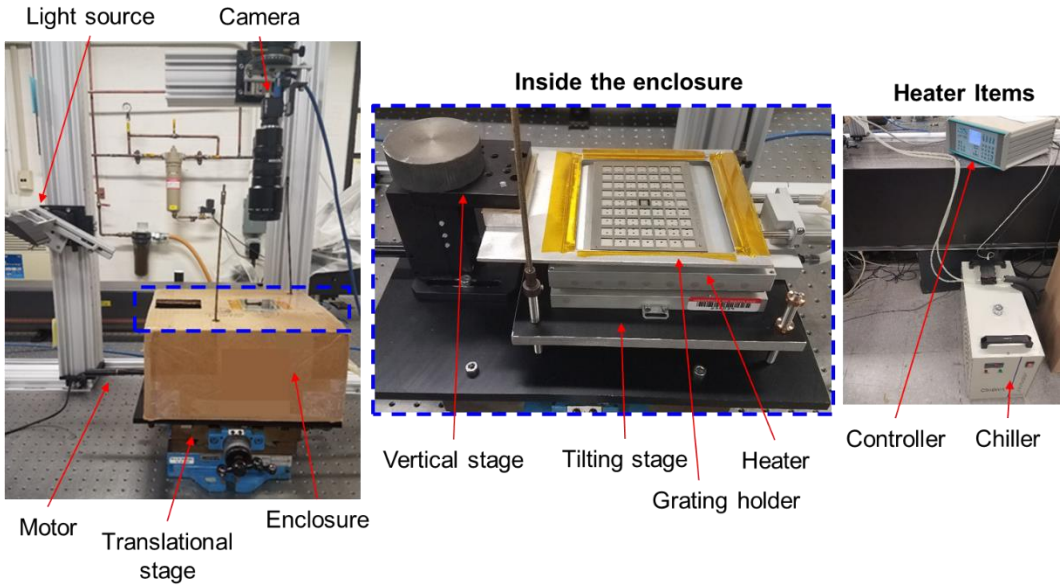

Figure 14. SM-NT Experimental Setup

As mentioned above, the three main ingredients of a shadow moiré setup are the camera, light source, and grating. A Blackfly USB3 Vision 2/3" format CCD camera (GS3-U3-28S5M-C) with 1920 x 1440 pixels was used as the imaging source. The light source was a Fiberoptic Systems quartz halogen 250W lamp with a 2.5 inch wide fiber optic line guide. Both were attached to a rotation stage so that α and β could be easily controlled. 0.25" thick Ronchii gratings made of fused silica with an additional blue chrome layer were obtained from Applied Image. The blue chrome is a thin layer of chrome oxide on top of the dark bars of the grating with very low reflectivity, minimizing potential interference from those regions.

The camera was used with two different lenses to account for different regions of interest. To image the whole strip, the Computar model M1614 mount lens was used. It is a 2/3" 16 mm F1.4 megapixel lens with a C-mount. The Navitar Zoom 7000 lens was used to image individual units due to its zooming capabilities. It is a 2/3" lens featuring a 6x magnification power with focal length from 18 to 108 mm and working distance from 5" to infinity, with a close-up lens.

A grating holder was fabricated out of thin aluminum to hold the grating in place. In order to enable fringe shifting, the grating holder was attached to a NP vertical positioner from J. A. Noll and actuated by a Thorlabs Z825B servo motor. The servo was controlled by the Thorlabs Advanced Positioning Technology (APT) software and has a 25 mm total travel distance with sub-micron resolution. The vertical positioner features a horizontal to vertical ratio around 2, so the servo displacement readings were roughly twice the grating holder displacements. The vertical positioner and attached grating holder were placed on top of a translational stage so that the imaging view could be changed without affecting the camera or light source.

The HCP306 hot and cold plate from Instec was used to bring the substrate to reflow temperatures. It features a 150 mm x 150 mm sample area with a range from -100 to 310 °C and a temperature uniformity of ±1.5 °C over the entire plate. The heating rate was sacrificed for its uniformity over the large area, as it features a maximum heating ramp rate of ~ 18 °C/minute. A box enclosure was used as additional insulation to help uniformity. The temperature uniformity within the jig, with the enclosure, was tested with thermocouples in the corners; as shown in Figure 15, the temperatures were very close, showing a max difference of 4 °C after reaching the

target temperature. Due to the ~6 °C difference between the set heater temperature and the thermocouple temperatures, the heater was set to 246 °C to account for this offset.

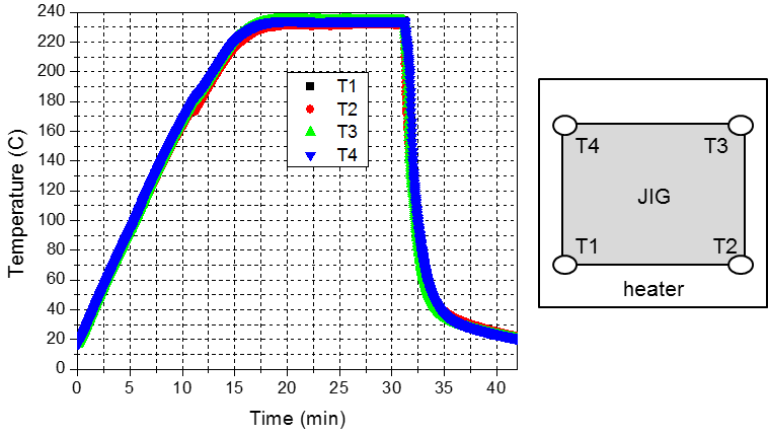

Figure 15. Jig temperature uniformity test

The heater was used in conjunction with an Instec mK1000 controller, C500WN10-AR chiller, and FVC11A fluid valve control box. The controller was the interface for the heater while the chiller and fluid valve box were used for temperature adjustments.

The heater was placed on top of a tilting stage, made of a ¾" thick black anodized flat plate and three 3" long ¼"-80 fine hex adjusters. Three ¼"-80 holes were tapped at 3 consecutive corners 7" away from each other, essentially creating a right triangle. By moving the position of the hex adjusters, the stage was able to tilt up to 18° in the x and y directions. This granted a large amount of flexibility regarding the specimens and their orientations during warpage measurements.

Warpages were measured with and without a magnetic jig used during the assembly process, which can be seen on top of the heater in Figure 14. Sized 120 mm x 95 mm, it is roughly half the size of the regular jig, due to the heater size. The jig is a combination of a flat bottom section made of aluminum with scattered magnets and

a top open grid section made of stainless steel. The top jig thickness was 0.7 mm, with an extra 0.3 mm for the positioning pins, while the bottom jig thickness was 3.8 mm.

The substrate of interest for this work was a 2 layer embedded trace substrate (2L ETS) for flip-chip chip scale packages (FCCSPs). The cross section for a portion of the substrate is shown in Figure 16. The substrate was arranged such that there were 7 x 19 unit substrates in a periodic structure within the entire strip, with each unit having the dimensions 11.9 x 9.6 mm. The total thickness of the substrate was 157 μm (the structure is described in more detail in Section 3). Each unit had 0.235 mm of additional material surrounding it on all four sides for handling and cutting purposes, which was referred to as the unit dummy. The unit dummy was excluded when measuring the warpage results for the unit.

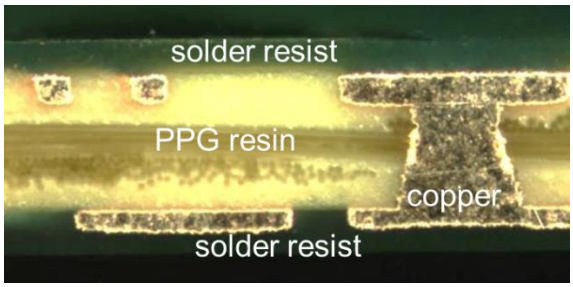

Figure 16. 2L ETS schematic

2.2.2. Setup Parameters

As discussed in the theory section, there are three parameters within the setup that govern the sensitivity of the shadow moiré experiment: α (light source incident angle), β (imaging source incident angle), and g (grating pitch). α was set at either 63.43° or 54.7°; 63.43° was used generally for increased sensitivity as tan(63.43°) = 2. If the imaging source incident angle was 0, using an α = 63.43° would double the

sensitivity. It offered a reasonable compromise between providing enough light to the specimen and increasing sensitivity. 54.7° was used in select cases to increase dynamic range as it maximizes Talbot distance, as shown in equation 11, and a longer Talbot distance increase the region with good contrast [34]. This was critical for being able to measure the warpage of the entire half-strip.

$$
\begin{aligned}
&D_T^{\alpha} = \frac{2g^2}{\lambda}\cos^3\alpha,\ \Gamma = \frac{g}{\tan\alpha} \\
&D_T^{\alpha} = \frac{\Gamma^2}{\lambda}\sin(2\alpha)\sin(\alpha) \\
&\frac{\partial D_T^{\alpha}}{\partial\alpha} = \frac{\Gamma^2}{\lambda}\frac{\partial[\sin(2\alpha)\sin(\alpha)]}{\partial\alpha} = \frac{\Gamma^2}{\lambda}2\sin\alpha(3\cos^2\alpha - 1) = 0 \\
&\therefore\ \alpha_c = 54.7^{\circ}
\end{aligned}
\tag{11}
$$

For the measurements conducted during this study, β was kept constant at 0°. Although increasing β results in increased sensitivity, β = 0° is the most convenient setting for imaging purposes and reduces any potential issues with unwanted reflections from the grating as well as the specimen. g is dependent on the available gratings; 5 and 10 lines/mm gratings (g = 0.2 and 0.1 mm respectively) were used.

Images were taken at both 0 and ½ Talbot distances, depending on the dynamic range necessary and the usage of the jig. As the warpages of unit substrates were small, 0 Talbot was used whenever possible for imaging substrates without the jig. However, as the height of the top jig and positioning pins were 0.7 – 1 mm, 0 Talbot distance was not attainable. The ½ Talbot distance for g = 0.1 mm and α = 63.4° is ~1.63 mm, so the dynamic range was insufficient for good contrast. As a result, all images of the substrate with the jig were taken at the ½ Talbot distance.

2.2.3. Calibration

A program in Labview was created to automatically move the grating holder down and take images with constant, but alterable phase differences. In order to calibrate the system, a 2.75" x 2.5" painted glass was used as an ideally diffuse specimen. 10 images were taken before and after the phase was shifted by 360°; the grating would move back to its original position when finished. The difference between the average gray values of each pixel from the average of the respective ten images were calculated at room and at reflow. A calibration factor was implemented to minimize the root-mean-square deviation (RMSD) at the two temperatures and was used for the measurements moving forward.

Because the positioner is mechanical, it is susceptible to backlash. To prevent this, the servo was programmed to move beyond its original position, and then inch back to its correct position. 10 images were taken at the initial and final positions, when the servo should be in the same position, to check for repeatability. The images had an average gray level difference of 0.88 and were deemed acceptable.

2.2.4. Effect of Paint

The biggest challenge associated with imaging the thin and advanced substrates stemmed from the inability to apply paint on the substrates. Because of the tiny substrate thickness, a 20-40 μm layer of paint cannot be ignored because it will substantially increase the rigidity and affect the substrate warpage. Two 3 x 3 sub-strips were used to test the effect of the paint on the warpage after reflow. They were subjected to a thermal cycle from room to reflow, where it was held for 15 minutes, and then returned to room temperature. From visual inspection, both showed clear

signs of convex shaped warpage. After paint was applied to one of the sub-strips, both were subjected to another thermal cycle.

The sub-strip that was left unpainted retained its convex shaped warpage. However, the painted sub-strip completely flipped its behavior and showed a concave shaped warpage, similar to a saddle. The deformations of the two sub-strips after the two cycles can be seen in Figure 17. This supplementary analysis reinforced the statement that paint on thin advanced substrates is significant; the lack of a diffuse surface has to be remedied through alternative methods. The next section will discuss the use of image processing to work around the challenges.

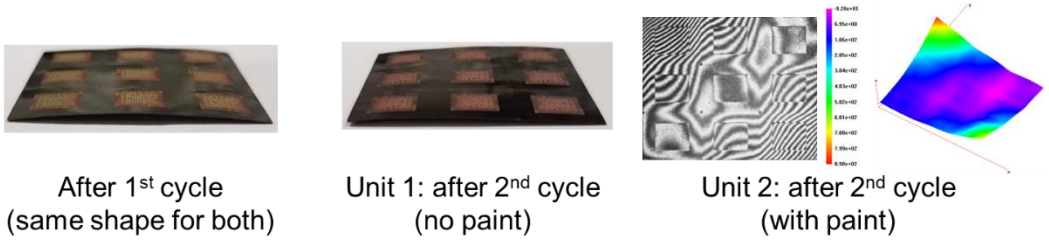

Figure 17. Effect of paint after thermal cycling

2.3. Fringe Analysis

2.3.1. Image Processing

There are two conventionally employed methods for processing shadow moiré fringes: phase shifting and optical/digital fringe multiplication (O/DFM). Both methods increase the sensitivity of the shadow moiré measurements, but attain them through different means. Phase shifting is a computer-reliant process that calculates fringe order at every pixel while O/DFM uses complementary images to increase its initial sensitivity by factors of 2.

The phase shifting technique was developed first. It uses a sequence of phase-shifted images to calculate fractional fringe orders based on harmonic fringe pattern intensities [35]. The intensity distribution is assumed to be sinusoidal and is expressed as

$$I(x,y) = I_m(x,y) + I_a(x,y)\cos[\phi(x,y)] \tag{12}$$

where:

$I_m(x,y)$ - mean intensity

$I_a(x,y)$ - modulation intensity

$\phi(x,y)$ - angular phase information of fringe pattern, related to the fringe order by

$$\phi(x,y) = 2N(x,y)$$

The three variables defined above are the three unknowns in the intensity equation, and can be solved with three equations from a known uniform phase shift. The most commonly employed algorithm uses a set of four phase-shifted images [36]

$$\begin{aligned} I_1(x,y) &= I_m(x,y) + I_a(x,y)\cos[\phi(x,y)] \\ I_2(x,y) &= I_m(x,y) + I_a(x,y)\cos[\phi(x,y) + \pi/2] \\ I_3(x,y) &= I_m(x,y) + I_a(x,y)\cos[\phi(x,y) + \pi] \\ I_4(x,y) &= I_m(x,y) + I_a(x,y)\cos[\phi(x,y) + 3\pi/2]. \end{aligned} \tag{13}$$

This enables the phase to be calculated as

$$\phi(x,y) = \arctan\left[\frac{I_4(x,y) - I_2(x,y)}{I_1(x,y) - I_3(x,y)}\right]. \tag{14}$$

This work has been extended so that the phase shifting technique can be applied when the phase shift is constant but unknown, or even arbitrary [36, 37].

One of the issues with phase shifting is that it implicitly assumes that shadow moiré fringes have a sinusoidal intensity distribution. The true intensity distributions

of these fringes are complex [37]. Han analyzed the errors associated with this assumption by comparing the sinusoidal assumption results with the results from the true intensity distribution. After experimental verification, it was found that the ideal maximum error associated with the assumption was approximately 1.7% of the contour interval [38]. This indicates that the error increases as the contour interval increases, so high basic measurement sensitivities are required for precise measurements.

The inherent phase shifting error was calculated for a painted diffuse surface. When applied to a non-diffuse surface, this error explicably increases as the differences between the phase shifted images will also include fluctuations from the surface. The copper regions of the units showed less than 10 μm of vertical warpage at reflow temperature. Therefore, with the basic contour interval of 50 μm, the phase shifting algorithm had to work with less than $1/5^{th}$ of a fringe order. With insufficient fringe information stemming from the low contour interval and the non-diffuse surface, phase shifting was unable to achieve the accuracy necessary. As a result, the image processing technique of choice was the O/DFM method.

The O/DFM technique uses a set of *n*-phase shifted images, but with a required phase difference of $2\pi/n$ between each image. By combining the images into a single pattern, a contour map with *n* times as many contours as the original can be created [39]. An example of the process for O/DFM2 *(n* = 2) is shown in Figure 18. In (a), two quasi-triangular intensity distributions with a π phase difference are shown. The absolute value of the differences between the intensities are taken, as illustrated in (b) and (c). The data is then truncated where $|I_r| = 0$ and binarized to create the sharpened intensity distribution in (d). This pattern has twice the number of fringes as the original

pattern. This algorithm can be extended for larger values of *n*, such as in (e), with *n* = 6.

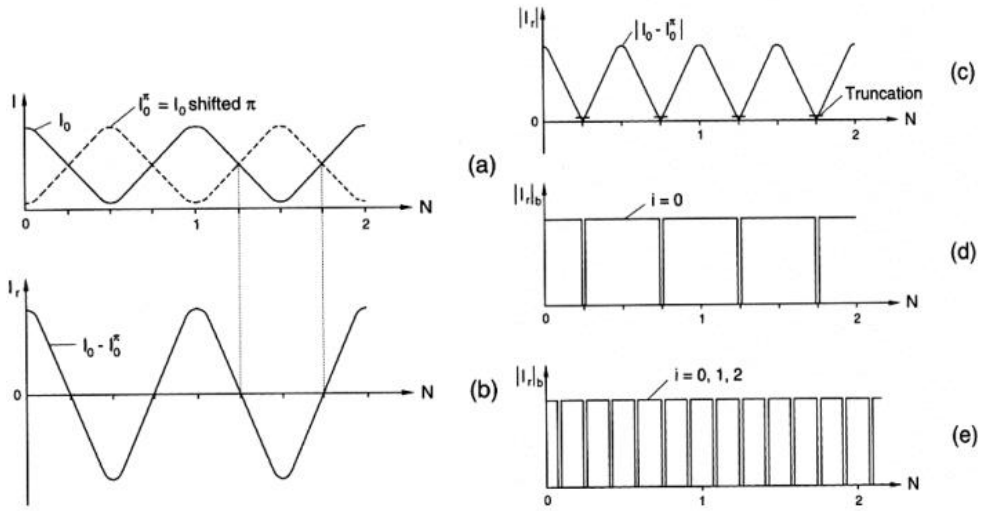

Figure 18. Steps in an O/DFM example with *n* = 2, 6

The practicality of this technique is exemplified by the images below. Figure 19 shows the moiré fringes of a plano-convex lens without and with O/DFM4, taken with a basic contour interval of 50 μm/fringe. The O/DFM4 (*n* = 4) enables the contour interval to be decreased by a factor of 4 to 12.5 μm/fringe.

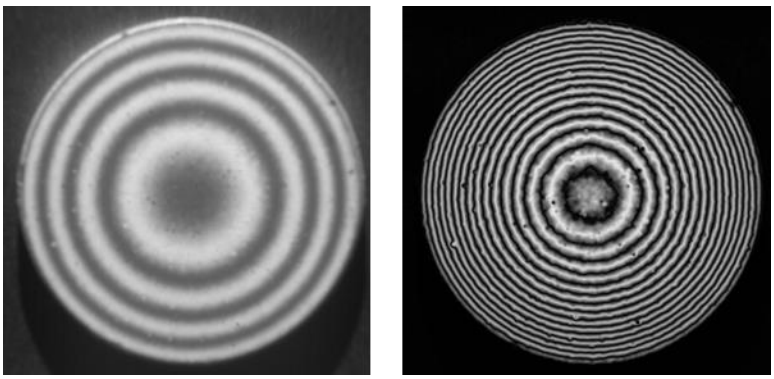

(a) (b)

Figure 19. Plano-convex lens without (a) and with (b) O/DFM4

One of the key advantages of the O/DFM algorithm, when compared to conventional processes such as phase shifting, is its ability to handle non-harmonic intensity distributions. It is important to recall that shadow moiré does not produce a harmonic intensity distribution, especially without paint. Regardless of the distributions, the subtractive process of O/DFM will always result in sharpened fringe contours. This is well suited for imaging objects with different surface properties, such as the substrate of interest with its outer solder resist (SR) and inner Cu regions on the top layer. Figure 20 shows the intensity distribution obtained from the middle horizontal line across the unit; the results clearly show the significantly different intensity distributions of the two regions.

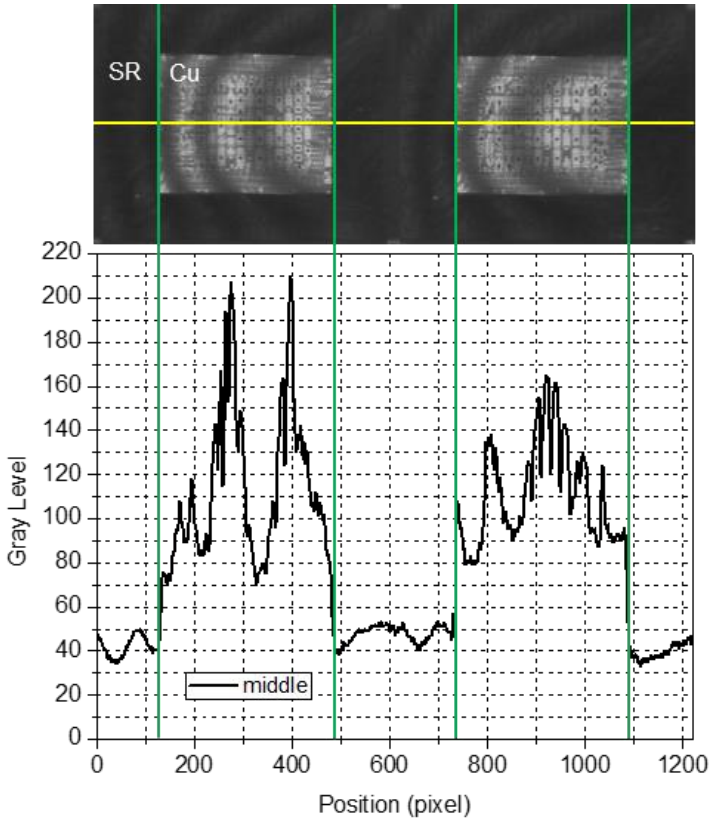

Figure 20. Intensity distribution comparison along the middle line between the SR and Cu regions for a tilted unit

The O/DFM algorithm can increase the sensitivity by *n*-fold provided there is enough intensity deviation between the initial and complementary images. Figure 21 illustrates this with a single substrate unit. The intensity distribution was obtained from the middle horizontal line across the three unit images: the unit with phase 0, its complementary unit with phase 180, and the resulting O/DFM2 unit. Despite the low and varying intensities within the outer SR region, the O/DFM process is able to easily discern where the subtracted intensities are 0 to successfully increase the sensitivity by a factor of 2.

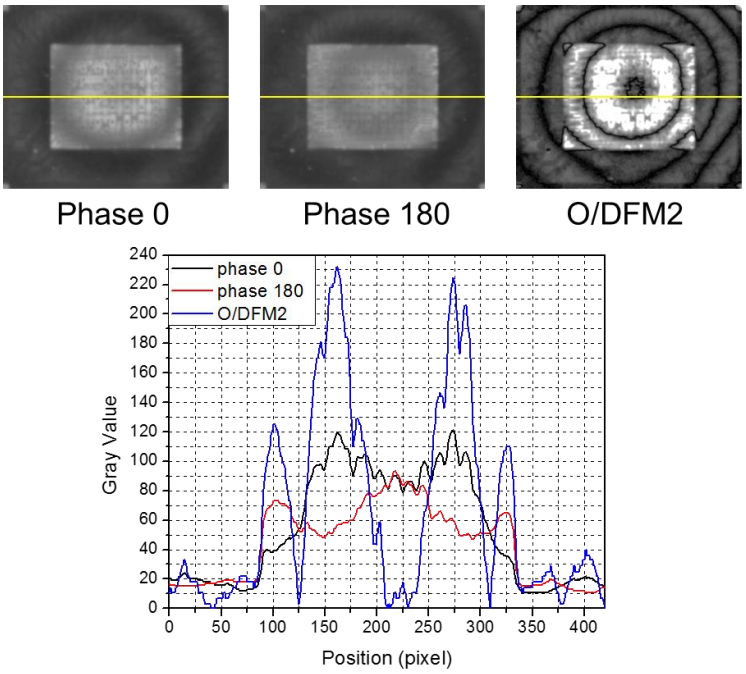

Figure 21. O/DFM2 schematic with varying intensity distributions

This stems from the fact that the O/DFM technique generally relies on data with the highest gradient of intensity versus fringe order, which is illustrated in Figure 22. Unlike the phase shifting technique of using data from all the pixels, O/DFM uses data from specific sites. The region used by O/DFM has a range of 0.45° while the data at

the maximum or minima have a range of 14.4°, producing a ratio of 32:1 [39]. It enables this technique to have high reliability even with non-simple harmonic distributions. Despite the intensity pattern variations in Figure 21 due to the trace patterns, O/DFM focuses on the intersecting data sites and can essentially neglect the majority of these variations when increasing sensitivity.

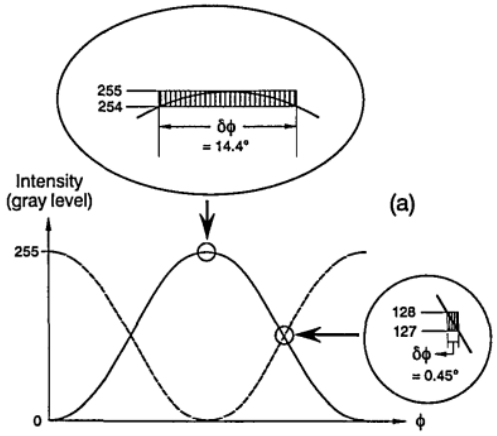

Figure 22. Data sites for simple harmonic intensity distribution [39]

2.3.2. O/DFM Results

Half of a representative strip was measured in a supplementary study to demonstrate the capabilities of the SM-NT system with unpainted substrates. Due to the large size and warpage of the half-strip, images were taken without the zoom lens, and with the parameters: g = 0.2 mm, α = 54.7°, and β = 0°. The critical camera angle of α = 54.7° was necessary to increase the dynamic range. Due to the large Talbot distance with g = 0.2 mm (5 lines/mm grating), using the ½ Talbot distance was not an option due to the low contrast from the aperture effect. The resulting large dynamic range enabled fringes to be captured at the 0 Talbot distance without any issues.

The fringes after O/DFM with $n = 4$ are shown in Figure 23; the cut-off unit to the right of the image is the center of the strip. Despite the lack of surface preparation, the fringes after O/DFM are extremely clear. The SM-NT system was robust enough to handle the large size and warpage of the strip with a post processing sensitivity of 35.4 μm/fringe. The quarter symmetry and periodic array of the middle row units close to the center can be observed.

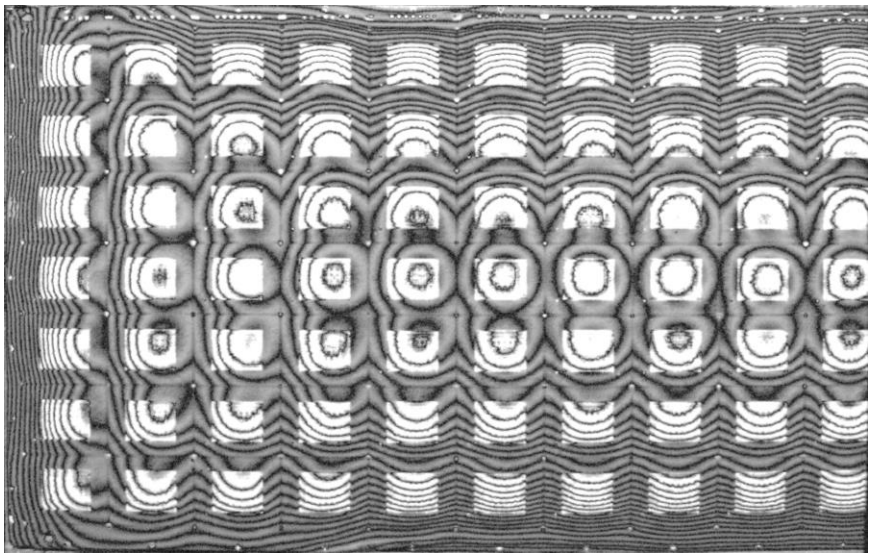

Figure 23. O/DFM4 fringes of the half-strip with $\Gamma = 35.4$ μm/fringe

For the hybrid model, the objective was to predict the warpage of substrate units with a metal jig at reflow temperature. Warpage values of the units were measured in 3 stages: at room without the jig, at room with the jig, and at reflow with the jig. The first two stages were used to obtain effective material properties and boundary conditions for model calibration, while the last stage was used to validate the model. 7 center units from different strips were chosen for the measurements at room without the jig because the center unit can be considered as the most representative unit due to

the periodic array of the strip. If the B.C. of the center unit is properly simulated, the warpage results can be compared directly with the model.

The 2nd and 3rd stages used 6 units from the half-strip above as representative units. Figure 24 shows the 6 units in relation to the left half-strip, with the center unit in black and the jig perimeter highlighted in blue. Because the jig encompasses an area just smaller than the half jig, the center units could not be chosen. 6 units close to the center, highlighted in red and numbered as shown from 1-1 to 2-3, were selected to minimize any potential temperature differences.

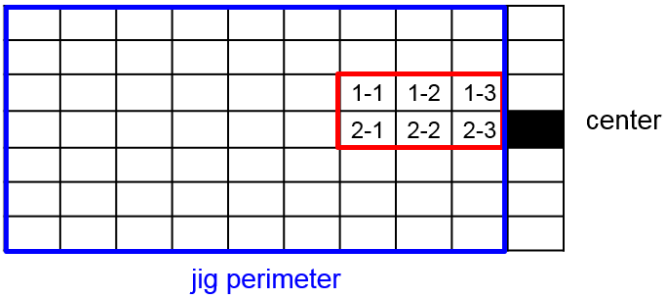

Figure 24. Locations of representative units from half-strip

A MATLAB code was used to find the locations of the fringes. The user first defines a reference line for the fringe locations. After specifying the real physical length of the line and manually pinpointing the fringe locations along the line, the code converts the pixel location into a real scale value. The fringe order at the beginning and start of the reference line was always defined, even if it was a fractional fringe order. Given the frequency of fringes, the accuracy of the fractional fringes at the ends can be estimated to be around 0.1 or less than 0.6 μm.

2.3.2.1. Unit Results at Room Temperature without Jig

The following three sections show the fringe patterns of units after O/DFM8 image processing and their respective warpages across the diagonals within the Cu region. O/DFM8 was implemented to reduce the base contour interval of 50 μm/fringe to 6.25 μm/fringe. The inner Cu region was the region of interest, and only the warpages within this area were considered as the jigs covered up the majority of the SR region. After the fringe locations were obtained from MATLAB and the fringe numbers were converted into warpage, the values went through rigid body rotation to ensure the warpage at the corners of the Cu regions were aligned. They were then offset by the warpage at the corners so that the warpage always started and ended at 0. Warpages along the diagonals were split into two, so that warpage was plotted from each corner to the center of the unit.

The fringes of the center units from 7 different strips after O/DFM8 are shown in Figure 25. Figure 26 displays the warpage data with respect to the normalized position along the diagonals of the Cu regions (path c) and the extrapolated maximum warpage values at the center. The shapes refer to the four different warpage paths from the corners to the center. The different colors represent the different units. The data shows reasonable scatter for experimental data.

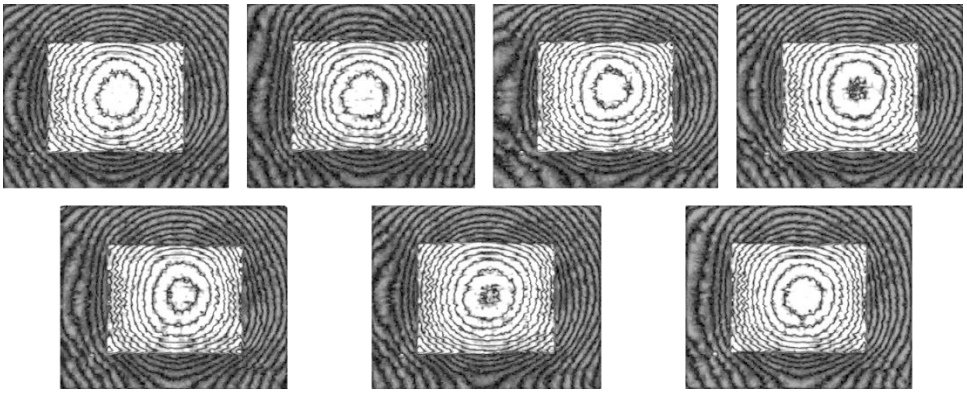

Figure 25. O/DFM8 fringes of 7 center units at room (Γ = 6.25 μm/fringe)

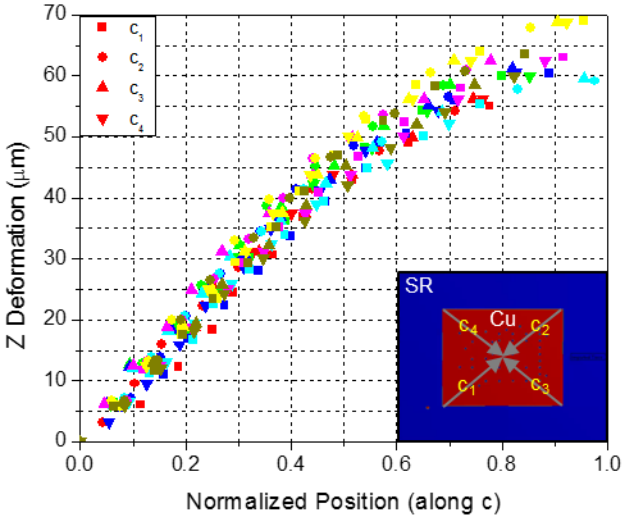

Warpage (μm)	Cu
Max	69.36
Min	58.89
Avg	63.34

Figure 26. Unit warpage values along the Cu diagonals at room

2.3.2.2. Unit Results at Room Temperature with Jig

The fringes of units 1-1 to 2-3 from section 2.3.2. after O/DFM8 are shown in Figure 27 with their respective warpages and max values shown in Figure 28. They

were measured at room temperature with the jig. The data also shows reasonable experimental scatter.

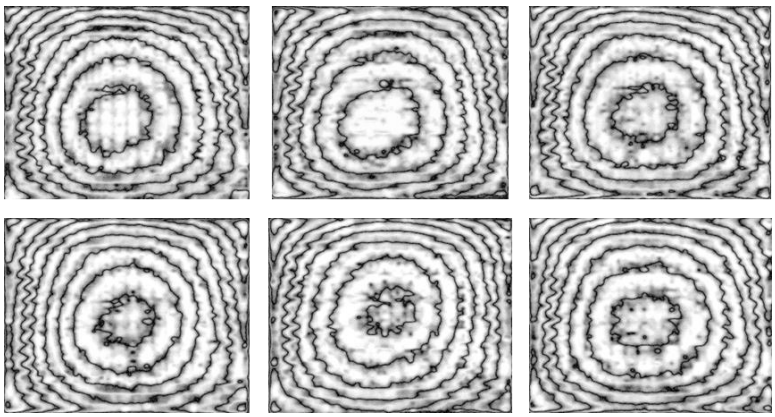

Figure 27. O/DFM8 fringes of the 6 units at room with jig (Γ = 6.25 μm/fringe)

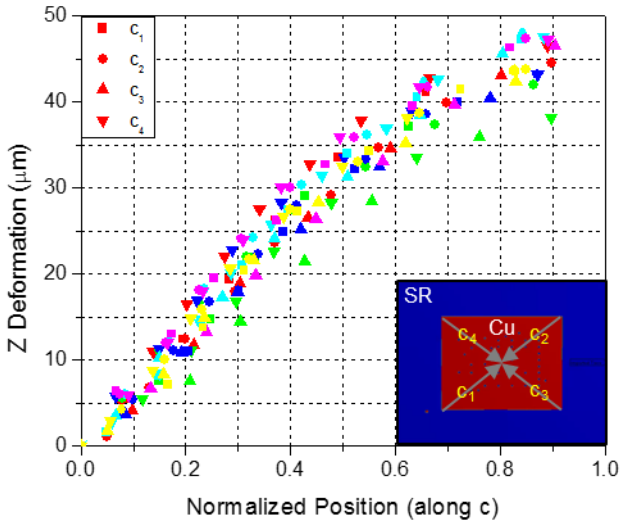

Warpage (μm)	Cu
Max	49.17
Min	38.65
Avg	45.40

Figure 28. Unit warpage values along the Cu diagonals at room with jig

2.3.2.3. Unit Results at Reflow Temperature With Jig

The fringes of the same units at reflow after O/DFM8 are shown in Figure 29 with their respective warpages and max values shown in Figure 30. They were

measured at reflow temperature with the jig. It should be noted that the data shows considerably more variation than the previous measurements.

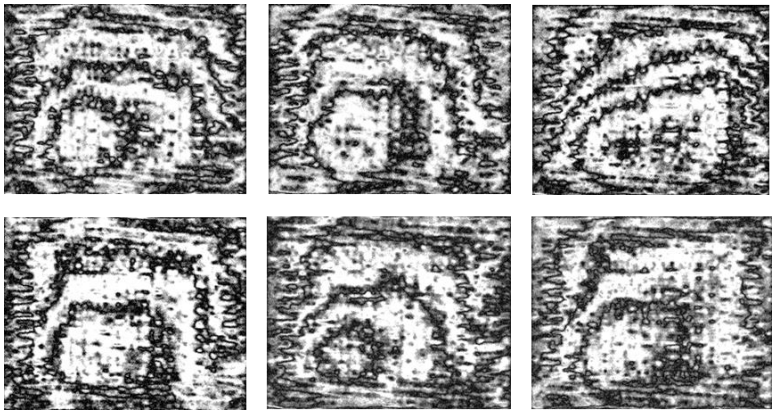

Figure 29. O/DFM8 fringes of the 6 units at reflow with jig (Γ = 6.25 μm/fringe)

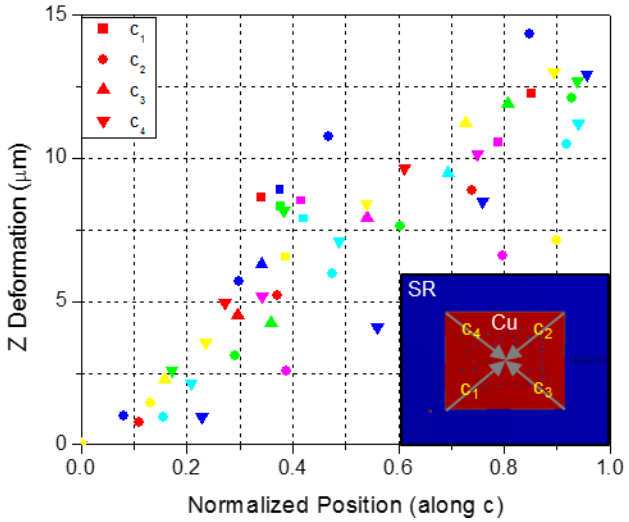

Warpage (μm)	Cu
Max	14.22
Min	7.54
Avg	11.49

Figure 30. Unit warpage values along the Cu diagonals at reflow with jig

These measurements served as the reference for the hybrid model.

Chapter 3: Modeling Advanced Substrates

3.1. Trace Mapping

3.1.1. General Procedure

Trace mapping is a recent technique developed by ANSYS to efficiently model complicated substrates. Modeling all of the complicated geometries within the substrate would require an immense amount of time. By incorporating the electronic computer-aided design (ECAD) directly into the simulation, trace mapping is able to significantly reduce the complexity of the problem without sacrificing accuracy. [40]

The procedure is completed in two steps, as shown in Figure 31. First, the ECAD is imported into the simulation as a rectangular grid (also called a source grid). Each unit is referred to as a "cell" and can be considered as the building block for the simulation. They contain the volume fraction information of each cell. The cell size should be dictated by the minimum feature size within the substrate and is controlled by the user during the import step. Then, after the user defines the geometry and mesh of the substrate layers, the source grid is overlaid on top of the target mesh. Effective material properties are assigned to elements encompassing cells, and results in a layer with accurate element material properties based on the actual trace layout. [40]

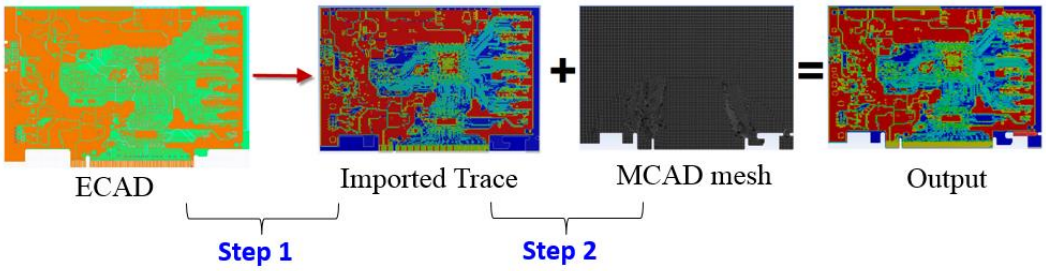

Figure 31. Trace mapping process [40]

3.1.1.1. Source Grid and Cells

Cells are the key to trace mapping; these rectangular units reflect the effect from microstructures. Because they are defined directly from the electrical trace layout, they accurately represent the substrate layers and can account for the effect of traces on the warpage. Figure 32 portrays step 1 of trace mapping; the ECAD data is imported and discretized as a grid.

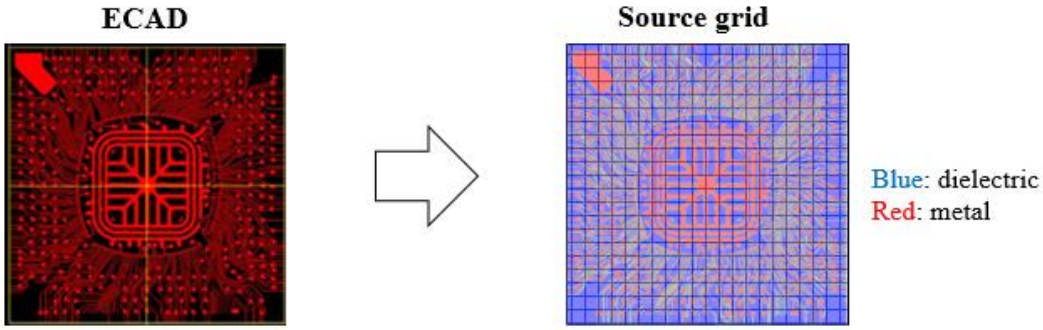

Figure 32. Source grid

There are three inputs during the import step: x/y discretization, thickness, and trace material. The x/y discretization controls how the layer information is sectioned, the thickness is the depth of the layer information, and the trace material defines the "metal." Trace mapping has the limitation that only two materials can be defined: a

"dielectric" and a "metal". As a result, the metal volume fraction of each cell is simply defined as the ratio between the metal and total cell area.

Refai-Ahmed et al. described how the volume fraction is used to define the properties of the cell [41]. Figure 33 is an example of a cell, where the blue region describes the metal region and the rest is dielectric material.

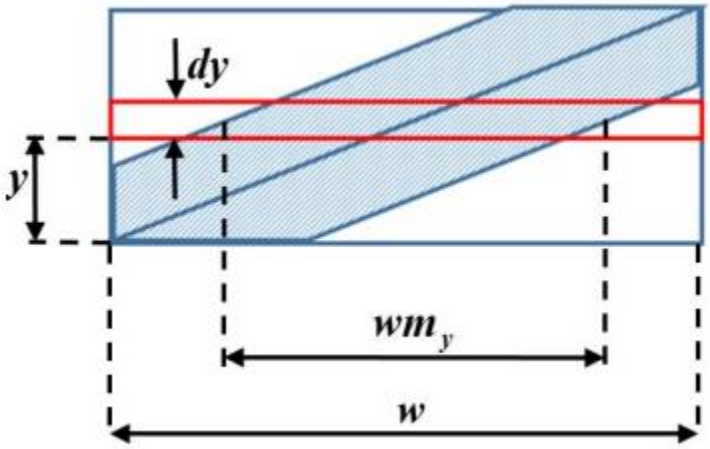

Figure 33 Cell example [41]

For a thin horizontal section across the cell, the metal volume fraction in the x-direction at height y can be described by [41]:

$$\frac{1}{E_x^y} = \frac{m_x^y}{E_x^M} + \frac{(1-m_x^y)}{E_x^D} \tag{15}$$

where:

E_x^y - effective Young's Modulus in the x-direction at height y

E_x^M, E_x^D - Young's Modulus in the x-direction at height y for the metal and dielectric materials, respectively

m_x^y - metal volume fraction in the x-direction at height y

This calculation uses the series combination of rule of mixtures, and assumes an isostress condition.

Assuming uniform strain, the effective Young's Modulus in the x-direction can be calculated by [41]:

$$F_x = \varepsilon_x \int_{y=0}^{y=h} E_x^y dy = E_x^{eff} h$$
$$E_x^{eff} = \frac{1}{h} \int_{y=0}^{y=h} E_x^y dy \tag{16}$$

ε_x is the uniform strain in the x-direction and h is the height of the cell. In this manner, effective material properties can be calculated in the x and y directions. Properties in the z direction are calculated through the parallel combination of rule of mixtures, assuming a constant metal volume fraction through the thickness. This value would be equal to the ratio between the area of the metal and the area of the entire cell.

3.1.1.2. Cell to Element Conversion

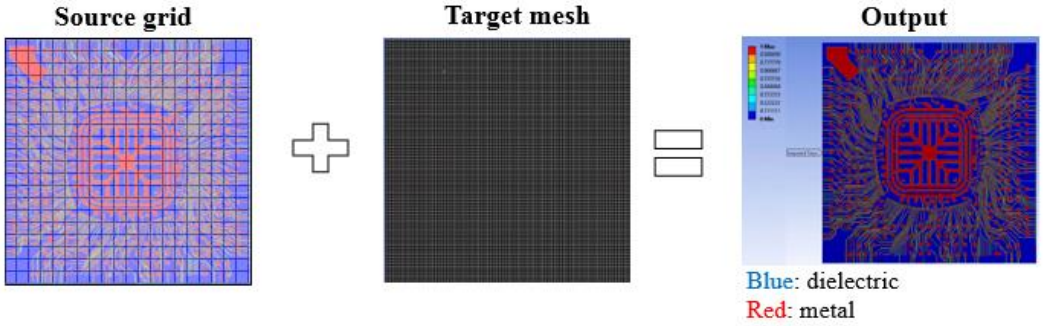

Figure 34. Combination of Source Grid and Target Mesh

The effective material properties of elements are designated from cell information during this procedure. As shown in Figure 34, the source grid is combined with the target mesh in order to evaluate the effective material properties of elements.

This process is further explained in Figure 35. First, the source grid is joined by the mechanical mesh. Then, the cells within an element act as a series-parallel network of springs to contribute to the effective material property [41]. Figure 35 (b) is a schematic of the spring network for calculating effect material properties in the x-direction. This incorporates the effect of each cell to the effective material property. A similar procedure is carried out for the y-direction material properties.

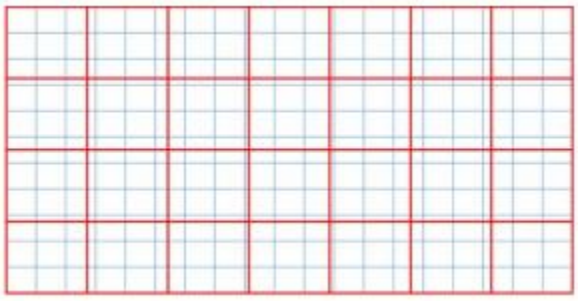

(a) Mesh (red) overlaid on the source grid (blue)

(b) Spring connections for effective element material properties in the x-direction

Figure 35. Cell to element conversion [41]

3.1.2. Trace Mapping Comparison

Examples in literature were used to gain further insight into how trace mapping compares with other modeling techniques. The general conclusion was that trace mapping has the potential to be very accurate because its effective element material properties are based directly on the mapped traces. However, this necessitates large

computational resources, and without small cells and elements, trace mapping's ability to define the layers correctly really struggles.

Yaddanapudi et al. analyzed the accuracy of three different techniques: lumped PCB model, detailed PCB model, and the trace mapped PCB model. The lumped PCB model is the simplest approach where traces are approximated through averaged uniform mechanical properties using volume fractions. The detailed PCB model was nearly the opposite as trace geometries were individually modelled and the trace mapped PCB model used trace mapping with a grid size of 400 x 400, which was chosen after a sensitivity study. When they compared stress and deformation values at four different locations within the board, it was found that the trace mapped PCB model matched the detailed PCB simulation very well. The average difference was less than 7% for the trace mapped model and was around 50% for the lumped model [42]. It was clear that the trace mapped model and its ability to capture material property variation within the layers enabled accurate predictions within the range of the detailed solid model simulation.

A study from another group compared trace mapping to zone-Cu% and layer-Cu% models, which divided the layers into regions and tried to match them with the actual design [5]. Zone-Cu% model assigns zones where each element is defined as a copper or non-metal through a randomization algorithm, but each zone matches the real Cu area density of that region. Layer-Cu% has the same material assignment algorithm but treats the entire layer as a single zone. Wang and Wells state that while trace mapping can be considered as the most reliable and consistent modeling schemes due to its ability to capture in-plane inhomogeneity and anisotropy, it has a high demand

for computational resources. The other two methods were nearly as accurate, but considerably simpler.

In both cases, trace mapping was identified as an accurate modeling scheme that provided reliable material properties without having to simulate all of the detailed traces. Although there are other simpler and more efficient modeling methods, trace mapping can combine the benefits of accurate material properties with enough averaging to avoid complexities associated with simulating all of the detailed traces. However, it requires large computational resources; and as seen from literature, trace mapping will contain errors without small cell/mesh sizes.

3.2. Unit Model

The unit model describes a 5 layer unit substrate within the 7 x 19 strip array, with dimensions 12.37 mm x 10.07 mm and total thickness of 0.157 μm. The unit dummy is included in the unit model but the simulation warpage results also excluded this region. The .bool version of the ECAD file for the single unit was used as the starting point. After being imported into the ANSYS Workbench model through trace mapping, the simulation was treated as a standard static structural model.

The goal of the unit model was to find the warpage of the units at the reflow temperature with the jig due to reliability concerns. The problem had the same approach as the experimental measurements; warpages were simulated in three different stages: at room, at room with jig, and at reflow with jig. The first model was used to determine the effective material properties, the second model was used to determine the effective boundary conditions, and the third model was the target.

3.2.1. Parameters

First, the geometry of the unit was created. A 5 layer solid model was formed with the described thicknesses and grouped into a single part, which forced adjacent layers to share the same nodes along the interface. This removed the need for contact elements. The names, materials, and thicknesses of each layer are displayed in Figure 36. "Filled" is the "metal" and indicates the trace material while "blank" is the "dielectric" and indicates the layer material. For solid models, the "dielectric" material is assigned to the layer and only the "metal" is specified within trace mapping. The .bool file also included extraneous FR4 layers, which were excluded from the analysis. The active layers and their trace materials are shown in Figure 37.

Layer	Material	File		Thickness (μm)
1	Air	S1	Filled	25
	Solder Resist (SR)		Blank	
2	Plated Cu (embedded)	M1	Filled	19
	PPG Resin		Blank	
3	Plated Cu (via)	D1	Filled	75
	PPG		Blank	
4	Plated Cu	M2	Filled	18
	SR		Blank	
5	Air	S2	Filled	20
	SR		Blank	

Figure 36. Layer structure

	Layer	Thickness (mm)	Trace Material	Active
1	S1_SOLDER	0.025	Air	☑
2	FR4	1E-20	PPG	☐
3	M1_COPPER	0.019	Copper Alloy	☑
4	FR4	1E-20	PPG	☐
5	D1_COPPER	0.075	Copper Alloy	☑
6	FR4	1E-20	PPG	☐
7	M2_COPPER	0.018	Copper Alloy	☑
8	FR4	1E-20	PPG	☐
9	S2_SOLDER	0.02	Air	☑

Figure 37. Imported trace interface

It was clear that the cell and mesh sizes are the two critical parameters for trace mapping and should be small enough to accurately describe the traces. For this particular substrate, the minimum trace width of the unit was 15 μm. Taking this into consideration, the cell and mesh size for the follow simulations were 15 μm, equal to the minimum feature size. The mesh size could not be reduced any further due to the available memory.

3.2.2. Boundary Conditions

The unit was modeled by taking the periodic structure of the strip into account. Although not perfect, the boundary conditions (B.C.'s) of the center unit should mimic the condition of periodicity (CoP), where all sides of the unit should remain as a vertical plane. The mathematical definition of CoP in relation to the faces of the unit is shown in Figure 38. In short, the unit may expand or contract, but without any change in the slope of the sides.

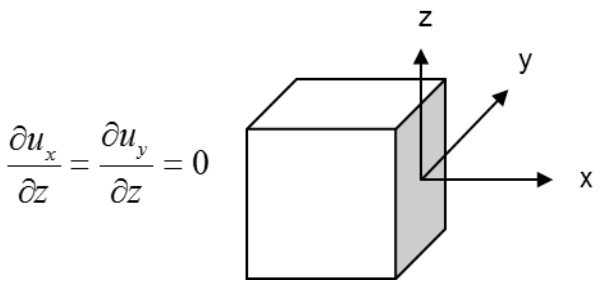

Figure 38. Unit reference for a "plane remains a plane" condition

This condition is valid provided that the unit has quarter symmetry. To check this assumption, the warpage along the diagonals for the traction free unit at room temperature was tested for symmetry. The only constraints placed on the substrate were constrained displacements at the corners to fix the 6 degrees of freedom. Informed that the stress free temperature of the substrate was roughly 268 °C, the simulation was run from 268 °C to 20 °C to describe the warpage at room. The warpages (normalized by the center warpage) along the four diagonals are plotted in Figure 39 and the FEM result is shown in Figure 40. The differences were less than 1% of the maximum warpage; these results confirm quarter symmetry, indicating that CoP is applicable.

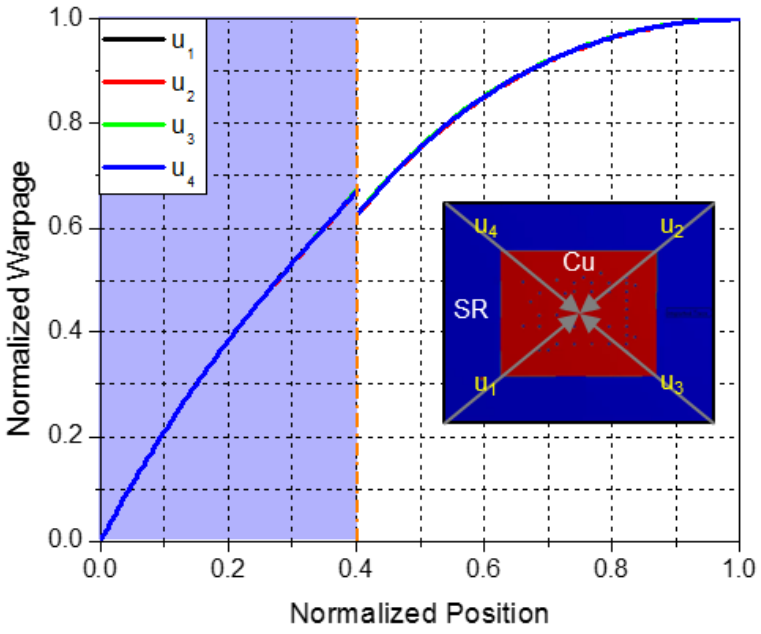

Figure 39. Verifying quarter symmetry for the traction free unit along the diagonals

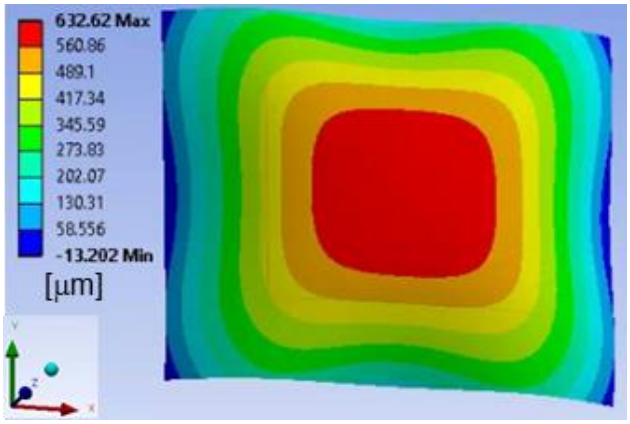

Figure 40. Traction free FEM unit model warpage (magnification x2.5)

The condition of periodicity was modeled through the use of coupled remote points in ANSYS. Selected geometries with the coupled conditions are forced to share selected DOF solutions. For example, if we consider a bimaterial joint with applied thermal loading, the joint will bend dependent on the material with higher coefficient of thermal expansion (CTE). The ends of the joint will be slanted. If the end faces

were coupled with respect to their normal, all of the nodes on those faces will be forced to have the same displacement in that direction. This effect is demonstrated in Figure 41, where the left and right ends of the coupled joint remain as a vertical plane. However, it is still free to expand transversely.

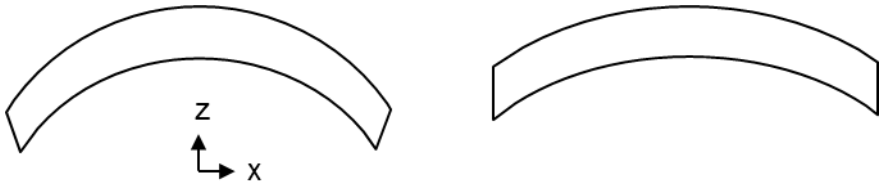

(a) (b)

Figure 41. Bimaterial joint (a) without coupling and (b) with coupling

Details of "Remote Point 4"	
Scope	
Scoping Method	Geometry Selection
Geometry	5 Faces
Coordinate System	Global Coordinate System
X Coordinate	6.185 mm
Y Coordinate	2.5e-002 mm
Z Coordinate	7.85e-002 mm
Location	Click to Change
Definition	
ID (Beta)	839
Suppressed	No
Behavior	Coupled
Pinball Region	All
DOF Selection	Manual
X Component	Active
Y Component	Inactive
Z Component	Inactive
Rotation X	Inactive
Rotation Y	Inactive
Rotation Z	Inactive
Pilot Node APDL Name	

Figure 42. ANSYS remote point selection

Figure 42 shows the ANSYS interface of the coupling condition applied on the right side of the unit model; the 5 faces were selected with the “coupled” behavior, with

the x component active. By applying the same condition on the left side and the top/bottom with respect to the y DOF, the condition of periodicity was applied to the unit model. As the coupling condition constrains x, y, and z rotation, the only other applied constraint forced the bottom left corner node to remain at (0, 0, 0) to prevent rigid body translation.

3.2.3. Initial Results

The unit model at room produced warpages significantly larger than the experimental data. Figure 43 shows the differences between the experimental warpage data and the uncalibrated FEM results at room; the simulation had roughly 3 times the warpage as the experimental data. This difference stems from the difficulty associated with perfectly modeling the conditions of the substrate. It is further confirmation of the necessity of the hybrid model, which will be discussed in the next section.

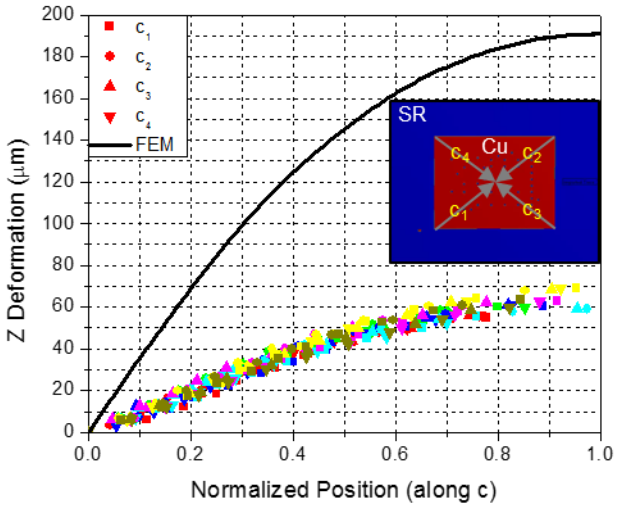

Warpage (μm)	Cu
Max	69.36
Min	58.89
Avg	63.34
FEM	190.92

Figure 43. Experimental warpage data with uncalibrated FEM results of units at room

Chapter 4: Warpage Prediction by Hybrid Method

4.1. Hybrid Method Approach

In the hybrid approach, the experimental results are used to tailor the properties, specifically material properties and boundary conditions, of the simulation. Figure 44 depicts the general layout of the hybrid approach, where the simulation and experimental results are compared during model calibration.

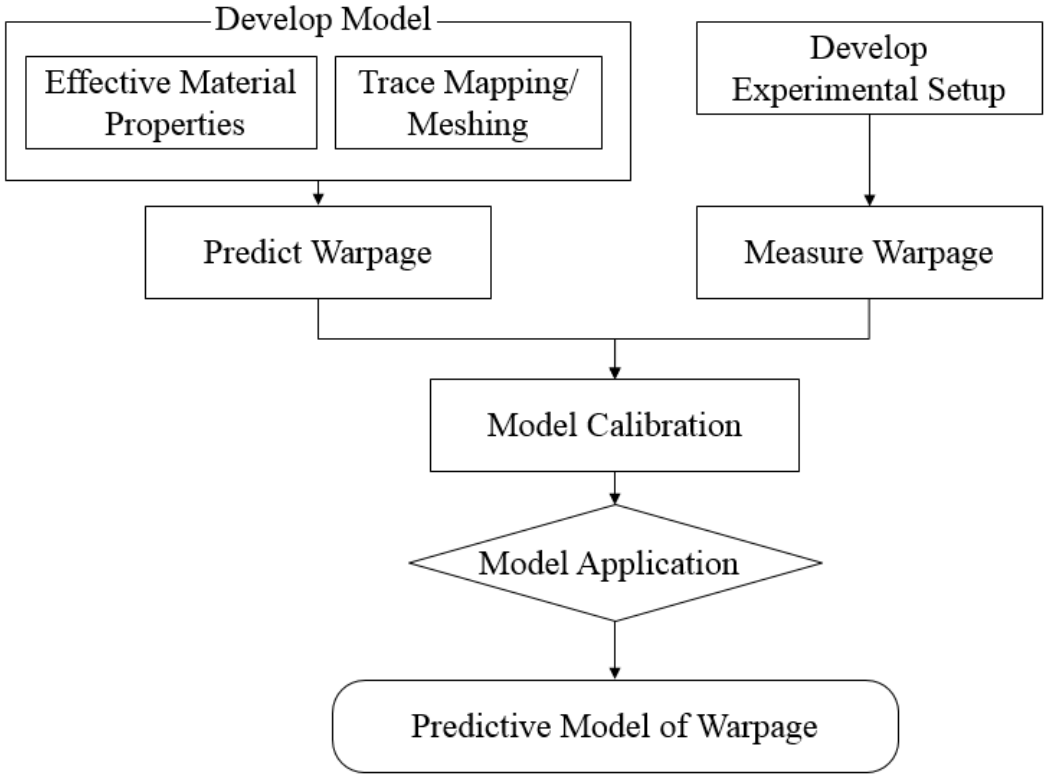

Figure 44. Schematic of the hybrid method approach

The parameters of the initial simulations are modified to match the experimentally obtained results, with emphasis on the materials properties and boundary conditions.

4.2. Implementation for the Unit Model

4.2.1. Model Calibration

In order to calibrate the model, a supplementary material property sensitivity study was conducted to identify the critical parameters. Warpages along the Cu diagonals of the unit model with CoP were evaluated with the modulus and CTE of Cu, PPG, and SR at 50 and 150% of their original values. Only a single parameter was changed each time so that the critical parameter could be deduced. The results of the sensitivity study are shown in Figure 45, with dashed lines representing material properties at 150% of their original value, and dotted lines for 50%. From this analysis, it was evident that the CTE of SR was the most critical parameter and was therefore selected for calibration.

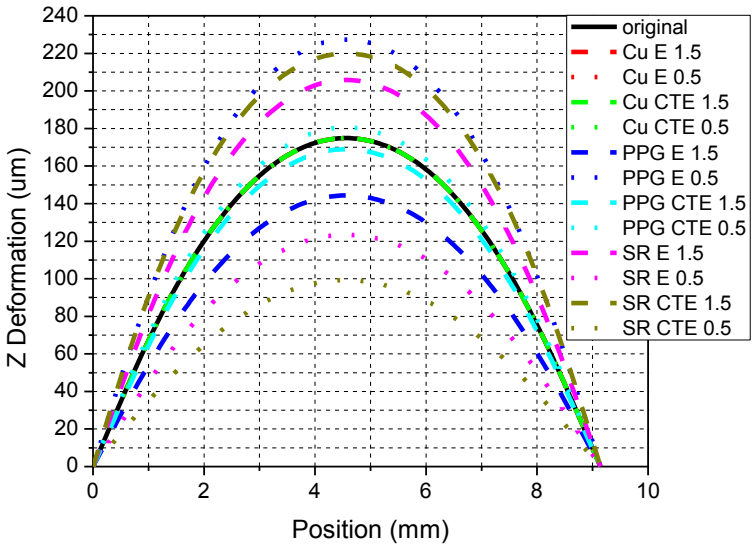

Figure 45. Material sensitivity study

As the initial unit model had significantly larger warpages than the experimental results, the CTE of SR was proportionally reduced until the RMSD between the

experimental data and simulation were minimized. The warpage and FEM results are shown in Figure 46 and Figure 47, respectively. The predicted values are a good fit and confirms the calibration of the unit model at room.

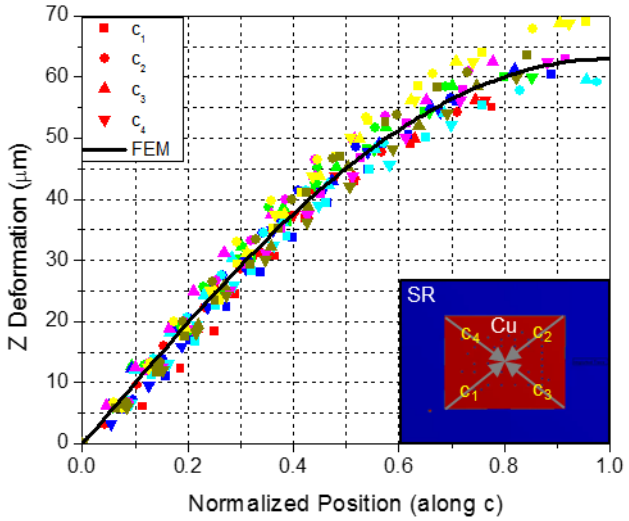

Warpage (μm)	Cu
Max	69.36
Min	58.89
Avg	63.34
FEM	62.99

Figure 46. Experimental warpage data with calibrated FEM results of units at room

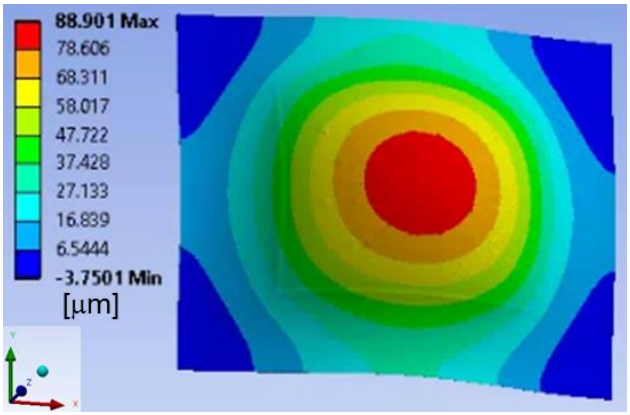

Figure 47. Warpage predictions of unit at room with calibrated material properties (magnification x 30)

4.2.2. Model Application

This simulation served as the baseline for the second stage, where the jig was introduced. The effect of the jig was modeled by setting zero displacement for the

nodes within the constrained region, matching the physical dimensions of the metal jig. This is illustrated in Figure 48. It prevented any warpage within the jig region, but left the middle region free to deform.

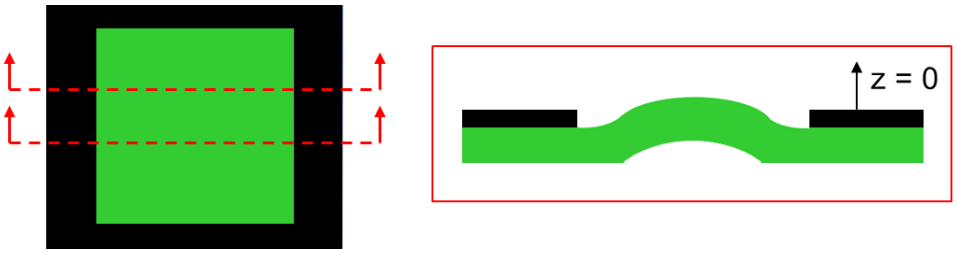

Figure 48. Simulated jig constraint

However, this condition was found to be over-constraining the substrate. The comparison of the simulation to the experimental data is shown in Figure 49.

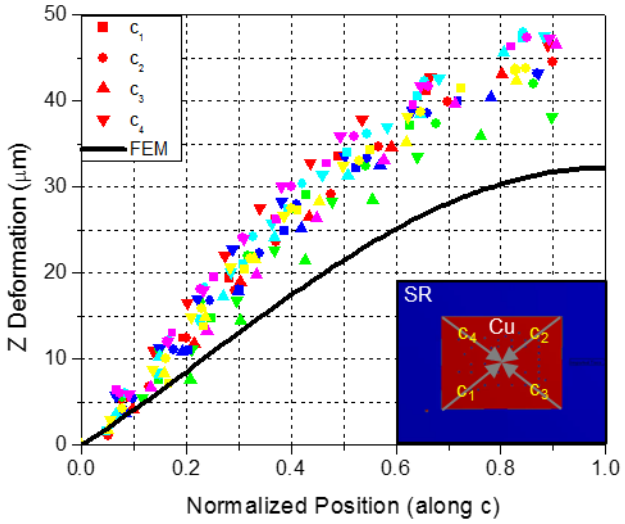

Warpage (µm)	Cu
Max	49.17
Min	38.65
Avg	45.40
FEM	32.20

Figure 49. Experimental warpage data with calibrated FEM results of units at room with jig

The ideal constraints of the jig within the simulation were not a correct reflection of the true conditions. The real effect of the jig was emulated by modifying

the simulated jig region. The parameters of the jig region were adjusted until the RMSD was minimized. The corrected prediction is shown in Figure 50 and its corresponding simulation result is shown in Figure 51.

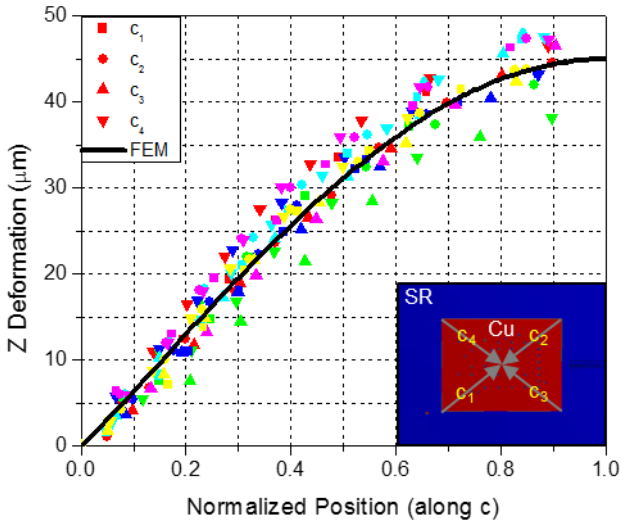

Warpage (μm)	Cu
Max	49.17
Min	38.65
Avg	45.40
FEM	32.20

Figure 50. Experimental warpage data with calibrated FEM results of units at room with modified jig constraints

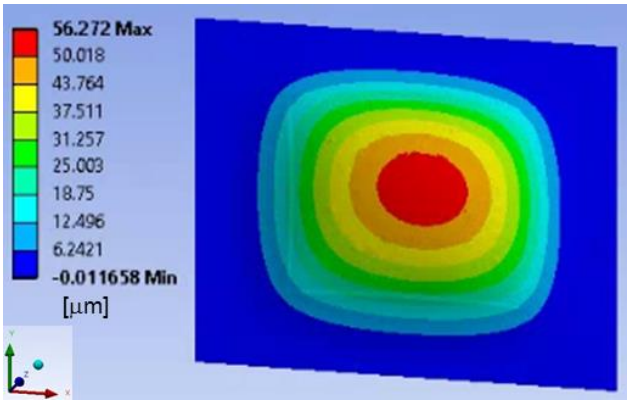

Figure 51. Warpage prediction of unit at room with calibrated material properties and modified jig constraints (magnification x30)

4.2.3. Predictive Model

The final step was to use the simulation with calibrated material properties and modified jig constraints to predict the warpage at the reflow profile. As the effective

properties and conditions of the model were obtained from experimental data, the simulation should be a reasonable match, even with different thermal conditions. The simulation was run from the stress free temperature of 268 °C to 240 °C. The warpage prediction is shown in Figure 52 and the corresponding simulation is shown in **Error! Reference source not found.**.

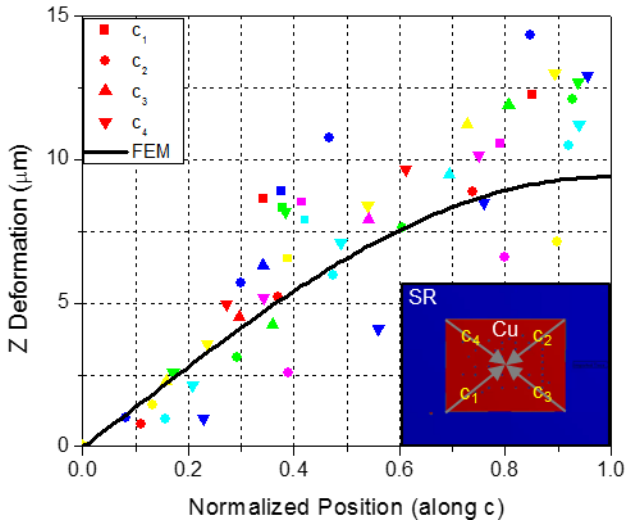

Warpage (µm)	Cu
Max	14.22
Min	7.54
Avg	11.49
FEM	9.40

Figure 52. Experimental warpage data with calibrated FEM results of units at reflow with corrected jig

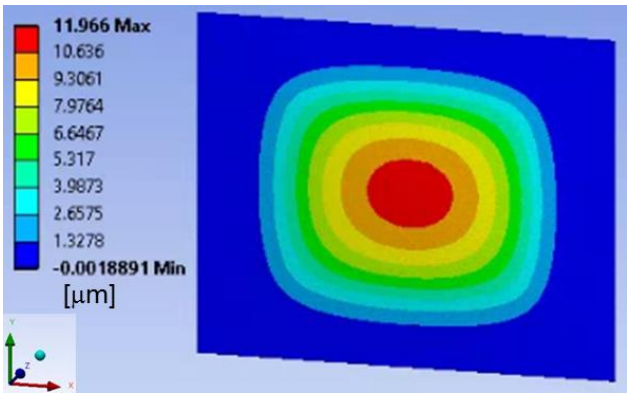

Figure 53. Warpage prediction of unit at reflow temperature with calibrated material properties and modified jig constraints (magnification x30)

The predicted values are well within the scope of the experimental results and verifies the applicability of the simulation as a predictive model of warpage for the substrate.

Chapter 5: Future Work

There were several additional avenues that can be explored in future work. The middle unit was measured and used for the simulation because of its closeness with the condition of periodicity. However, units will have progressively different boundary conditions the closer they are to the boundary, particularly the corner and edge units. Given that the condition of periodicity is for an infinitely long periodic array, there is no guarantee that the units within the middle 5 rows can be assumed to have the "plane remains a plane" condition. Creating specific boundary conditions for different regions, such as the middle, corner, and edge, would enable a better understanding of the unit substrate warpages within the strip.

In addition, the parameters of trace mapping relied on the minimum feature size due to recommendations from ANSYS and references from literature. The effective element material properties are dependent on the cellular directional fractions, but their physical meanings are proprietary. An in-depth analysis of the effect of the cell using ideal reference traces is in the plan for future work so that the true relationship between the cells and effective element properties can be understood.

Another direction that will be explored is the warpage prediction of the entire strip. Although the SM-NT setup was robust enough to handle the dynamic range and sensitivity necessary, there was no corresponding model. Attempts were made, but the strip model showed extremely deviant behavior regardless of various changes. Use of the high computing cluster at Maryland (Deepthought2) will be utilized for running the model with fine elements.

Finally, the effect of manufacturing variations is another aspect to explore with the capability of the SM-NT setup and the trace mapping simulations. The measurements and simulations assumed that the parameters of the substrate were ideal and therefore, used the ideal specified values. However, manufacturing variability is inherent in all systems, and using the setup to address these issues would have been a viable possibility.

Chapter 6: Conclusion

The advent of thin and advanced substrates necessitates accurate modeling schemes to predict their warpages. A hybrid model was proposed and implemented to predict the warpage of these thin substrates. In the method, an advanced SM-NT technique was used to experimentally measure the warpages of units without the use of paint. These measurements were used to tailor the material properties and the conditions for the unit model with jig at reflow temperatures. With the accurate experimental data, the hybrid model was able to mimic the conditions of the unit while taking the layout of the microstructures into consideration. The results confirmed that the proposed model is an effective tool to predict the warpage of advanced substrates at reflow temperature.

Bibliography

[1] F. P. Carson, *et al.*, "3-D Stacked Package Technology and Trends," *Proceedings of the IEEE*, vol. 97, p. 12, 2009.

[2] P. Chen, *et al.*, "Warpage Prediction Methodology of Extremely Thin Packages," presented at the 67th Electronic Components and Technology Conference, Orlando, FL, 2017.

[3] W. Lin and M. W. Lee, "PoP/CSP Warpage Evaluation and Viscoelastic Modeling," presented at the Electronic Components and Technology Conference, Lake Buena Vista, FL, 2008.

[4] F. Lee, *et al.*, "Ultra Thin Substrate Assembly Challenges for Advanced Flip Chip Package," presented at the 13th International Wafer Level Packaging Conference, San Jose, California 2016.

[5] M. Wang and B. Wells, "Substrate Trace Modeling for Package Warpage Simulation," presented at the 66th Electronic Components and Technology Conference, Las Vegas, NV, 2016.

[6] R. S. Khandpur, *Printed Circuit Boards*: Tata McGraw-Hill Education, 2005.

[7] Dahl. (2016, December 18). *Printed Circuit Board CAD System*. Available: http://www.islaywhiskyclub.com/category/pcb-manufacturing/

[8] B. Han and P. Kunthong, "Micro-Mechanical Deformation Analysis of Surface Laminar Circuit in Organic Flip-Chip Package: An Experimental Study," *Journal of Electronic Packaging*, vol. 122, p. 7, 2000.

[9] Y. Tsukada, *et al.*, "Surface Laminar Circuit Packaging," presented at the Electronic Components and Technology Conference, San Diego, CA, 1992.

[10] Y. Tsukada, "Chapter 9: Solder Bumped Flip Chip Attach on SLC Board and Multichip Module," in *Chip on Board*, J. H. Lau, Ed., ed: Van Nostrand Reinhold, 1994, pp. 410-443.

[11] J. H. Lau, "Recent advances and new trends in flip chip technology," *Journal of Electronic Packaging*, vol. 138, p. 030802, 2016.

[12] Y. Sun, *et al.*, "Development of Ultra-Thin Low Warpage Coreless Substrate," presented at the Electronic Components and Technology Conference, Las Vegas, NV, 2013.

[13] M. Kurashina, *et al.*, "Low Warpage Coreless Substrate for Large-Size LSI Packages " presented at the Electronic Components and Technology Conference, San Diego, CA, 2012.

[14] W. Lin, *et al.*, "Coreless Substrate with Asymmetric Design to Improve Package Warpage," presented at the Electronic Components and Technology Conference, Orlando, Florida 2014.

[15] J. Kim, *et al.*, "Warpage Issues and Assembly Challenges Using Coreless Package Substrate " presented at the IPC APEX EXPO 2012.

[16] W. Lin, "A Feasible Method to Predict Thin Package Actual Warpage Based on an FEM Model Integrated with Empirical Data," presented at the Electronic Components and Technology Conference, San Diego, 2015.

[17] M. Kurashina, *et al.*, "Low Warpage Coreless Substrates for IC Packages," *Transactions of The Japan Institute of Electronics Packaging*, vol. 5, p. 8 2012.

[18] F. Kraemer, *et al.*, "The Effect of Copper Trace Routing on the Drop Test Reliability of BGA Modules " in *Electronic Components and Technology Conference* Las Vegas, NV, 2010.
[19] N. Vijayaragavan, *et al.*, "Package on Package Warpage - Impact on Surface Mount Yields and Board Level Reliability," presented at the Electronic Components and Technology Conference, Lake Buena Vista, FL, 2008.
[20] F. Carson, *et al.*, "Controlling Top Package Warpage for POP Applications," in *Electronic Components and Technology Conference*, Reno, NV, 2007.
[21] B. Willis and D. Bernard, "The Challenges of Package on Package (PoP) Devices During Assembly and Inspection," in *SMTA International*, San Diego, 2009.
[22] J. Zheng, *et al.*, "Relative and Absolute Warpage Modeling on Molded Packages," presented at the Electronic Components and Technology Conference, San Diego, CA, 2015.
[23] B. Zhang, *et al.*, "Modeling of Board-Level Package by Finite Element Analysis and Laser Interferometer Measurements " *Microelectronics Reliability,* vol. 50, p. 7, 2010.
[24] D. M. Meadows, *et al.*, "Generation of Surface Contours by Moiré Patterns," *Applied Optics,* vol. 9, p. 6, 1970.
[25] H. Takasaki, "Moiré Topography " *Applied Optics,* vol. 9, p. 6, 1970.
[26] D. Post, *et al.*, *High Sensitivity Moire: Experimental Analysis for Mechanics and Materials*. New York: Springer-Verlag, 1994.
[27] K. C. Yuk, *et al.*, "Determination of the absolute order of shadow moiré fringes by using two differently colored light sources " *Applied Optics,* vol. 33, p. 3, 1994.
[28] J. A.Gómez-Pedrero, *et al.*, "Measurement of surface topography by RGB Shadow-Moiré with direct phase demodulation " *Optics and Lasers in Engineering,* vol. 44, p. 13, 2006.
[29] S. Song, *et al.*, "Warpage measurement of various substrates based on white light shadow moiré technology," presented at the Microsystems, Packaging, Assembly and Circuits Technology Conference, Taipei 2011.
[30] B. Kwong, "Advanced Shadow Moiré with Non-Conventional Imaging Angles," Master of Science, Department of Mechanical Engineering, University of Maryland, College Park, College Park, 2012.
[31] H. F. Talbot, "LXXVI. Facts relating to optical science. No. IV " *The London and Edinburgh Philosophical Magazine and Journal of Science,* vol. 3, p. 7, 1836.
[32] M. Testorf, *et al.*, "Talbot effect for oblique angle of light propagation," *Optics Communications,* vol. 129, p. 6, 1996.
[33] C. Han and B. Han, "Contrast of shadow moiré at high-order Talbot distances " *Optical Engineering,* vol. 44, p. 6, February 2005 2005.
[34] C. W. Han, "Shadow Moiré Using Non-Zero Talbot Distance and Application of Diffraction Theory to Moiré Interferometry " Doctor of Philosophy, Mechanical Engineering, University of Maryland, College Park, 2005.
[35] K. Creath, "Phase-measurement interferometry techniques " *Progress in Optics,* vol. 26, p. 50, 1988.

[36] Z. Wang, "Development and application of computer-aided fringe analysis," Doctor of Philosophy, Department of Mechanical Engineering, University of Maryland, College Park, 2003.
[37] H. Du, *et al.*, "Algorithm for phase shifting shadow moiré with an unknown relative step " *Journal of Optics*, vol. 13, 2011.
[38] C. Han and B. Han, "Error analysis of the phase-shifting technique when applied to shadow moiré " *Applied Optics*, vol. 45, p. 10, 2006.
[39] B. Han, "Interferometric methods with enhanced sensitivity by optical/digital fringe multiplication," *Applied Optics*, vol. 32, p. 6, 1993.
[40] ANSYS®, "Academic Research Mechanical, Release 17.2, Help System, ECAD Analysis using Trace Mapping, ANSYS, Inc. ," ed.
[41] G. Refai-Ahmed, *et al.*, "Electronic PCB and Package Thermal Stress Analysis," presented at the 66th Electronic Components and Technology Conference, Last Vegas, NV, 2016.
[42] V. K. Yaddanapudi, *et al.*, "Validation of New Approach of Modelling Traces by Mapping Mechanical Properties for a Printed Circuit Board Mechanical Analysis," presented at the Electronics Packaging and Technology Conference, Singapore, 2015.